J. Seidl, Manfred Aigner, Roman Keller, Peter Gerlinger, CFD Simulations of turbulent nonreacting and reacting flows for rocket engine applications, The Journal of Supercritical Fluids Volume 121, 2017, 63-77.

The original publication is available at www.elsevier.com

http://dx.doi.org/10.1016/j.supflu.2016.10.017

CFD simulations of turbulent nonreacting and reacting flows for rocket engine applications

Martin J. Seidl [a], Manfred Aigner [b]

Institute of Combustion Technology,

German Aerospace Center (DLR), 70569 Stuttgart, Germany

Roman Keller [c], Peter Gerlinger [d]

Institute of Combustion Technology for Aerospace Engineering,

University of Stuttgart, 70569 Stuttgart, Germany

A consistent real gas framework based on a preconditioning scheme is implemented into the CFD code TASCOM3D to simulate nonreacting and reacting turbulent flows with transcritical injection. All thermodynamic properties and partial derivatives are rigorously evaluated from the reduced residual Helmholtz energy by use of fundamental thermodynamic relations. The Soave-Redlich-Kwong equation of state with an optional volume translation is employed in combination with high-pressure models for the calculation of fluid transport properties. Three test cases are simulated to validate the implemented real gas framework using different turbulence modeling strategies. A good match between numerical and experimental data is obtained.

Keywords:

real gas, transcritical injection, rocket combustion chamber, CFD, DDES, preconditioning

[a] PhD Student (Corresponding author, E-mail address: martin-janos-seidl@web.de)

[b] Professor, Head of Institute

[c] PhD Student

[d] Apl. Professor

Nomenclature

Latin symbols

a, b, c	parameters in SRK EOS
$\mathcal{A}, \mathcal{B}, \mathcal{C}$	mole number based parameters in SRK EOS
a_s	isentropic speed of sound
A	Helmholtz energy
c_p , c_v	specific heat at constant pressure / volume
d	diameter
$D_{\alpha\beta}$	diffusion coefficient of species α in β
e_tot	specific total energy
f	frequency
f_β , f_a	scaling function in preconditiong and AUSM$^+$-up scheme
h_tot	specific total enthalpy
k	modeled turbulent kinetic energy
L	length
Ma	Mach number
M_w	molecular weight
n	mole number
p	pressure
q	turbulence variable $q = \sqrt{k}$

r	radius
R_u	universal gas constant
T	temperature
u	velocity
v_m, V	molar and extensive volume
X, Y	mole and mass fraction
y^+	normalized wall distance

Greek symbols

α	temperature-dependent term in SRK EOS
β	preconditioning factor
λ	thermal conductivity
μ , μ_t	molecular and turbulent viscosity
ρ , ρ^*	density and normalized density
Ψ	reduced residual Helmholtz energy
ω	transport variable in turbulence models
ϖ	acentric factor

Vectors and tensors

$\mathbf{Q}_\mathrm{c}$	conservative variable vector
$\mathbf{Q}_\mathrm{p}$	primitive variable vector
$\mathbf{F}$, $\mathbf{F}^\nu$	inviscid and viscous flux vector

$\mathbb{\Gamma}$	preconditioning matrix
$\mathbb{J}$	Jacobian matrix
$\mathbb{S}$	source term vector
$\mathbb{T}$	transformation matrix

Subscripts, superscripts, and accents

inj	values within injector or at its end
m	mole based property
r	residual property
$\breve{}$	partial density property
$\hat{}$	partial mass property

Acronyms

AUSM	advection upstream splitting method
BKC	Brennkammer C (combustion chamber C)
CFD	computational fluid dynamics
DDES	delayed detached eddy simulation
DNS	direct numerical simulation
EOS	equation of state
FRC	finite-rate chemistry
IG	ideal gas

IWRCM-2	2nd International Workshop on Rocket Combustion Modeling
LES	large eddy simulation
LHS	left-hand side
LOX	liquid oxygen
LU-SGS	lower-upper symmetric Gauss-Seidel
MLP^{ld}	multidimensional limiting process low diffusion
RANS	Reynolds-averaged Navier-Stokes
RHS	right-hand side
SRK	Soave-Redlich-Kwong
SRK-C	Soave-Redlich-Kwong with volumen translation factor c
TVD	total variation diminishing
URANS	unsteady RANS

1 Introduction

1.1 Motivation

Supercritical flows, i. e. flows in which the pressure exceeds the thermodynamic critical pressure of the fluid, play a major role in several industrial applications, e. g. in process, petroleum, and nuclear engineering [1–3]. Due to increasing efficiency with higher pressures, supercritical conditions are also encountered in many large scale rocket engines. For example, the Vulcain II engine of Europe's civil rocket Ariane V operates at about 115 bar [4]. This is far above the critical pressures of the propellants H_2 and O_2, which are at about 13 and 50 bar.

Though the combustion chamber pressure exceeds the critical pressure of the propellants in many current main and future upper stage rocket engines, injection temperatures, at least of O_2, are often cryogenic below the critical temperature (about 155 K for O_2). This is often termed a transcritical state or injection, resp. [5, 6]. During the process of heat-up, transcritically injected fluids transit the so-called pseudo-boiling or widom-line, resp., which connects the states of divergence in the specific heat at constant pressure [6,7]. The transition from a liquid-like to a gas-like state is characterized by strong variations of fluid properties like density, specific heat at constant pressure, viscosity, and thermal conductivity [1,8]. The locally resultant strong spatial gradients constitute a great challenge for computational fluid dynamics (CFD) simulations in terms of accuracy and stability.

Modeling of high-pressure thermodynamics and fluid properties demands modifications of the numerical framework. Real gas equations of state (EOS) and transport property models must be implemented, a variety of which can be found in literature [8]. The goal of this

study is to simulate turbulent flows with transcritical injection relevant for rocket engines by employing a real gas extension, which was recently implemented into the in-house CFD code TASCOM3D.

1.2 Literature study

Understanding the complex phenomena involved in supercritical flows is a major goal of experiments concerned with transcritical injection without [9–16] or with [9, 17–21] combustion. Due to increasing computing powers, supercritical mixing and combustion processes are also in increasing focus of relatively recent numerical studies employing steady-state Reynolds-averaged Navier-Stokes (RANS) simulations [11, 22–34], large eddy simulations (LES) [5, 28, 35–42], or even direct numerical simulations (DNS) [43–46].

Apart from turbulence modeling, a diversity of physical and numerical models is applied in these simulations. For modeling the thermodynamic behavior, simple and efficient cubic equations of state like the Soave-Redlich-Kwong (SRK) or the Peng-Robinson EOS are usually preferred due to their general validity and to limit computational costs, e. g. [28, 36, 41]. However, highly accurate EOS like the modified Benedict-Webb-Rubin EOS were also implemented for simulations of single component flows [33, 36, 40]. Thermodynamic properties are mostly calculated at runtime, but may alternatively be obtained from precalculated look-up tables [33, 40], which is faster, though hardly applicable for general mixtures, since the dimensionality of the table increases with the number of considered species. Combustion models in use comprise chemical equilibrium, e. g. [22, 47], flamelet, e. g. [25, 29–33, 40], or detailed finite-rate chemistry (FRC) approaches, e. g. [5, 35–37]. Either pressure-based solvers with compressibility extensions, e. g. [28–31], or density-based solvers including preconditioning

techniques, e. g. [5, 24, 35, 36], are applied.

To validate numerical models, reliable experimental data are required. However, available data sets from transcritical injection experiments are very limited due to difficult measurement conditions in high pressure (and in case of combustion also high temperature) environments. In this study, one nonreacting and two reacting test cases are investigated numerically. The first two test cases were already widely studied in literature by CFD.

At first, the disintegration of a turbulent, transcritically injected N_2 jet into a warm N_2 environment at a pressure of 40 bar is studied. Associated experiments were conducted by the group of Mayer at the DLR site in Lampoldshausen [10, 13] and proposed as validation test case "RCM-1" at the 2nd International Workshop on Rocket Combustion Modeling (IWRCM-2) [48]. Ever since it was extensively studied in numerical simulations using RANS [11, 22, 23, 26–28], LES [28, 38, 40–42], and 2D-DNS [46] techniques.

The second test case, also proposed as a validation test case at this workshop [49], is a rectangular model rocket combustor with a single element shear coaxial injector operated at about 65 bar by ONERA at its test facility MASCOTTE [18, 20, 21]. Numerical studies for this H_2 - O_2 combustion test case termed "A-60" are exclusively 2D-axisymmetric RANS simulations [6, 24, 29–33, 47, 50–53] except for 3D-RANS calculations presented in [34].

The third test case is a round model rocket combustor termed "BKC" with a single element shear coaxial injector operated by DLR in Lampoldshausen at about 60 bar [54, 55]. Again, propellants are H_2 and O_2. Experimental results at various operating conditions have only partially been published yet and, to the authors' knowledge, no numerical investigations have been published so far.

1.3 Synopsis

For the simulation of the aforementioned test cases, a thermodynamically consistent real gas framework was implemented into a preconditioning scheme similar to Zong and Yang [5]. In contrast to other CFD codes, all thermodynamic properties and partial derivatives are rigorously calculated from the reduced residual Helmholtz energy by fundamental thermodynamic relations valid for any fluid and EOS. This procedure, as proposed by Michelsen und Mollerup [56], is very flexible and efficient.

In this study, the SRK EOS with an optional species-dependent, but otherwise constant volume translation is used. For the calculation of high-pressure transport properties, various models from literature where implemented and compared. Different turbulence modeling strategies are under study: steady-state RANS and unsteady RANS (URANS) simulations based on two-equation models as well as a hybrid URANS / LES approach from Spalart [57] named DDES (delayed detached eddy simulation). A high order discretization technique up to fifth order in space in combination with a multi-dimensional limiting process from Kim and Kim [58] in the version of Gerlinger [59], called MLP^{ld}, and the AUSM^{+}-up flux splitting method from Liou [60] is utilized to obtain accurate results and a robust numerical scheme in the presence of excessively large spatial gradients.

The main part of this article is organized as follows: First, the new real gas thermodynamic module is presented in section 2. Subsequently, the governing equations and numerical scheme of the applied CFD code TASCOM3D are presented in section 3. Necessary modifications for real gas simulations at arbitrary Mach numbers are outlined. Afterwards, the numerical results for the three test cases are presented and discussed in detail in sections 4 - 6. A

conclusion summarizes the main outcomes.

2 Thermodynamics

2.1 Equation of state

For high-density fluids at high pressures and low to moderate temperatures, the classical ideal gas (IG) law is no longer valid and has to be replaced by a real fluid EOS. The choice of an appropriate EOS depends on the desired application and is usually a balance between general validity, accuracy, and computational efficiency. In this study, the simple, but efficient SRK EOS with an optional species-specific, but otherwise constant volume translation (SRK-C) is employed. Its accuracy was found to be sufficient for the intended applications. The SRK-C EOS for pure fluids can be written in the form of

$$
\begin{aligned}
p &= \frac{R_\mathrm{u} T}{\acute{v}_\mathrm{m} - b} - \frac{a(T)}{\acute{v}_\mathrm{m}\,(\acute{v}_\mathrm{m} + b)} \quad \text{with} \quad v_\mathrm{m} = \acute{v}_\mathrm{m} - c\,, \qquad (1)\\
a(T) &= a_\mathrm{cr}\,\alpha(T),\ \alpha(T) = \left[1 + \kappa\left(1 - \sqrt{T/T_\mathrm{cr}}\right)\right]^2 + \varepsilon_\alpha\\
\text{and } \kappa &= 0.480 + 1.574\,\varpi - 0.176\,\varpi^2\,.
\end{aligned}
$$

A discussion of the correction factor ε_α is given later in this section. The EOS parameters $a_\mathrm{cr} = a\,(T = T_\mathrm{cr})$ and b are determined from the critical temperature and pressure of the fluid [8]. The volume translation factor c is zero in the original SRK EOS.

Péneloux et al. [61] proposed a correction method, which can be applied to any pressure-explicit EOS. They introduced a volume translation method, which shifts the calculated molar volume $\acute{v}_\mathrm{m} = \acute{v}_\mathrm{m}(T, p)$ by a constant factor c to obtain the physical molar volume v_m. This may greatly improve predicted molar volumes for liquids and transcritical fluids, whereas gaseous densities remain almost uneffected.

In case of mixtures, the EOS parameters are obtained from classical mixing and combining

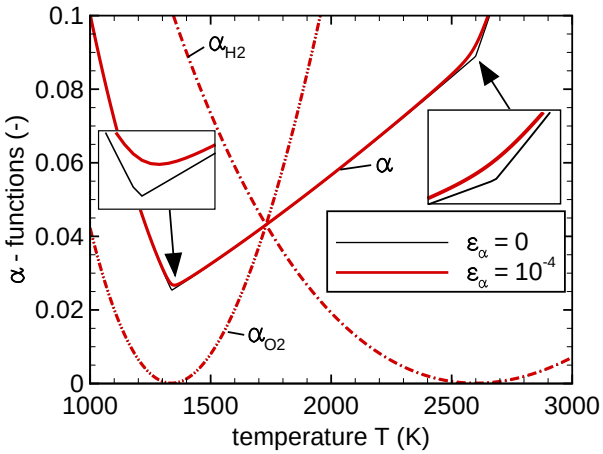

Figure 1: Pure fluid α-functions of H_2 and O_2 as well as α-function of an equimolar H_2 - O_2 mixture without ($\varepsilon_\alpha = 0.0$) and with ($\varepsilon_\alpha = 10^{-4}$) correction.

rules from their pure fluid counterparts (species index α) [8]:

$$a = \left(\sum_{\alpha=1}^{N_{\mathrm{sp}}} X_\alpha \, a_\alpha^{1/2} \right)^2 = \frac{1}{n^2} \left(\sum_{\alpha=1}^{N_{\mathrm{sp}}} n_\alpha \, a_\alpha^{1/2} \right)^2 , \tag{2}$$

$$b = \sum_{\alpha=1}^{N_{\mathrm{sp}}} X_\alpha \, b_\alpha \qquad = \frac{1}{n} \sum_{\alpha=1}^{N_{\mathrm{sp}}} n_\alpha \, b_\alpha , \tag{3}$$

where n and n_α are total and species mole numbers and $X_\alpha = n_\alpha / n$ species mole fractions in a mixture of N_{sp} components. The mixture parameter for c is calculated analogously to b.

The constant correction factor ε_α in Eq. (1) was set to 10^{-4}. It is not included in the original SRK EOS but was introduced to attain a continuously differentiable α-function not only in the case of pure fluids but also mixtures, which otherwise might result in numerical problems under certain circumstances. Figure 1 shows α-functions for H_2 and O_2 as well as for an equimolar mixture of both. Though the pure fluid α-functions are continuously differentiable, the mixture α-function without correction is not at high temperatures, where the pure fluid α-functions become zero.

Significant deviations from the ideal gas behavior for the investigated test cases are mainly

expected in regions, where the injected fluids remain at cryogenic temperatures. Densities and molar specific heats at constant pressure $c_{p,\mathrm{m}}$ for the relevant fluids N_2, O_2, and H_2 calculated with the IG, SRK, and SRK-C EOS are therefore compared in Fig. 2 to correlations from REFPROP [62], a thermodynamics database software from NIST. The arrows in the left picture of Fig. 2(b) indicate the corresponding y-axis for the different lines. Clearly, the IG law is unsuited at very low temperatures. The SRK does a good job for all three considered fluids. Only for N_2, larger deviations are observed for densities at very low temperatures. The predictions down to temperatures of about 123 K can be improved with a volume shift of $c = +7.0 \cdot 10^{-6}$ m^3/mol for test case 1.

2.2 Derived thermodynamic properties

The applied numerical scheme involves the calculation of several thermodynamic properties like specific heats, speed of sound, and partial mass enthalpies, but also of partial derivatives like $\partial\rho/\partial p$, $\partial\rho/\partial T$, and $\partial\rho/\partial Y_\alpha$ with Y_α the mass fraction of species α. These can be derived from the EOS based on fundamental thermodynamic relations valid for arbitrary fluids and any EOS. The derivations are straight forward, but may become tedious for complex EOS. In the case of two-phase flows, local thermodynamic equilibrium is assumed, though only single-phase flows are studied in this work. Basic concepts in the applied procedure are thermodynamic potentials, residual functions, and partial properties [56], which will briefly be introduced next.

A thermodynamic potential is a quantity, which contains all thermodynamic information of a system and from which all other thermodynamic properties can be derived rigorously by partial derivatives via fundamental thermodynamic relations. Examples for thermodynamic

potentials are the inner energy E, enthalpy H, as well as Gibbs energy G and Helmholtz energy A, the latter two having the most practical relevance. The residual function of a variable ϕ is defined as $\phi^{\mathrm{r}} := \phi - \phi^{\mathrm{IG}}$, where ϕ^{IG} is the contribution of a hypothetical ideal gas at the same temperature, volume, and composition. Residual functions may not be confused with the analogous concept of departure functions also often found in literature, where the ideal gas part is evaluated at the same pressure instead of volume. Partial molar and partial mass properties of a species α in a mixture are defined by partial derivatives of the associated extensive variable $\Phi = n\,\phi_{\mathrm{m}} = m\,\phi$ with respect to species mole numbers n_α or masses m_α at constant temperature, pressure, and mole numbers or masses, resp., of all other species: $\check{\phi}_\alpha := (\partial\Phi/\partial n_\alpha)|_{T,p,\{n_{\beta\neq\alpha}\}}$ and $\hat{\phi}_\alpha := (\partial\Phi/\partial m_\alpha)|_{T,p,\{m_{\beta\neq\alpha}\}}$, where $\{...\}$ indicates a row vector. Both intensive quantities are related via $\check{\phi}_\alpha = M_{\mathrm{w}}\,\hat{\phi}_\alpha$.

Since the concepts involve extensive properties like mole numbers n_α and volume $V = n\,v_{\mathrm{m}}$, the CFD code, however, is based on intensive properties mass fractions Y_α and density ρ, a connection has to be established between both frameworks. Meng and Yang [35] developed the concept of partial density properties and derived a relation between those and partial mass properties. Their framework requires partial derivatives with respect to species densities $\rho_\alpha := Y_\alpha\,\rho$, which becomes complicated for more complex EOS than the applied SRK EOS.

An alternative procedure is derived in this work following Michelsen and Mollerup [56]. They calculate all derived properties from the reduced residual Helmholtz energy Ψ via partial derivatives with respect to temperature, volume, and mole numbers. Their method is applicable to any EOS given in pressure-explicit form $p = p\,(T, v_{\mathrm{m}}, \{X_\alpha\}) = p\,(T, V, \{n_\alpha\})$ or in its Helmholtz form $A = A\,(T, V, \{n_\alpha\})$, straightforward also for complex EOS, and can be implemented in a modular, flexible, and efficient way.

If an EOS like the SRK EOS is given in its pressure-explicit form, the first step consists in evaluating the reduced residual Helmholtz energy from

$$\Psi(T, V, \{n_\alpha\}) := \frac{A^\mathrm{r}(T, V, \{n_\alpha\})}{R_\mathrm{u} T} = -\frac{1}{R_\mathrm{u} T} \int_\infty^V \left[p(T, V', \{n_\alpha\}) - \frac{n R_\mathrm{u} T}{V'} \right] \mathrm{d}V' \,. \tag{4}$$

This is easy for the SRK and SRK-C EOS, though it can be a more difficult task for complex EOS. For the IG EOS, Ψ is zero of course. Inserting the SRK-C EOS into Eq. (4) yields:

$$\Psi^\mathrm{SRK-C} = n \ln\left(\frac{V}{V + \mathcal{C} - \mathcal{B}}\right) + \frac{\mathcal{A}}{R_\mathrm{u} T} \frac{1}{\mathcal{B}} \ln\left(\frac{V + \mathcal{C}}{V + \mathcal{C} + \mathcal{B}}\right) \tag{5}$$

with $\mathcal{A} = n^2\, a$, $\mathcal{B} = n\, b$, and $\mathcal{C} = n\, c$. The partial derivative of pressure with respect to temperatur at constant volume and composition can then for example be calculated from

$$\left(\frac{\partial p}{\partial T}\right)_{V, \{n_\alpha\}} = -R_\mathrm{u} T \left(\frac{\partial^2 \Psi}{\partial T\, \partial V}\right)_{\{n_\alpha\}} + \frac{p}{T} \,. \tag{6}$$

The complete set of derived properties is presented in the appendix.

2.3 Fluid property modeling

At high densities, transport properties like viscosity μ, thermal conductivity λ, and binary mass diffusion coefficients $D_{\alpha\beta}$ exhibit similar deviations from the ideal gas behavior like thermodynamic properties as density and specific heats. Strong variations occur especially around the critical point. This requires the use of models developed for real gas conditions, i. e. high pressures and low temperatures. Models should be efficient, general valid for pure substances and mixtures, and accurate enough for the intended applications. A variety of models can be found in common literature, e. g. in the textbook of Poling et al. [8].

For CFD simulations of flows with transcritical injection, either the models of Ely and Hanley [63, 64] or of Chung et al. [65] are commonly used. For the prediction of binary mass

diffusion coefficients, Takahashi's model [66] is widely excepted in the community. We have scrutinized these models together with alternative models from Huber and Hanley [67] (for μ and λ) as well as Riazi and Whitson [68] (for $D_{\alpha\beta}$). Both models' advantage in contrast to the established models is that they only provide deviations from the ideal gas behavior similar to residual functions presented previously. In the limit of low densities (ideal gas) they reduce to the underlying ideal gas models for pure fluids and mixtures. This is not true for the models of Ely and Hanley as well as Chung et al., which are stand-alone models.

We have also found some unphysical behavior for the models of Ely and Hanley, Chung et al., and Takahashi. For very high temperatures (say greater than 3000 K), which may occur in rocket combustion chambers, there is an unphysical deflection to higher values for the viscosity and thermal conductivity in the model of Ely and Hanley. The model of Chung et al. is not applicable to species with negative acentric factor like hydrogen. This deficiency can at least partially be remedied by limiting the acentric factor to non-negative values in this model. The Takahashi model was found to predict unphysical, sometimes even negative values at very high pressures and low temperatures.

A comparison of various models with experimental values for the ideal gas viscosities in H_2 - H_2O mixtures and high-pressure binary mass diffusion coefficients of H_2O in supercritical CO_2 is presented in Fig. 3. At ideal gas conditions, the model of Wilke [69] valid for ideal gases is close to experimental viscosity data from Huang et al. [70] (Fig. 3(a)). The method of Huber and Hanley [67] will produce good results in this case, since it reduces to the model of Wilke in the ideal gas limit. The models of Ely and Hanley as well as Chung et al., however, cannot reproduce ideal gas values accurately in this case for large mole fractions of H_2O. At high-pressure conditions, the model of Huber and Hanley [67] is often close to correlations

from REFPROP for both viscosity and thermal conductivity. A comparison with REFPROP correlations is given in Fig. 4. For highly polar fluids like H_2O, deviations are more significant on the liquid side and close to the critical point.

Taking a look at calculated high-pressure diffusion coefficients (Fig. 3(b)), the ideal gas model of Fuller et al. [71] clearly overpredicts the experimental values from Xu et al. [72]. The model of Riazi and Whitson is much closer to the experiment. As mentioned previously, the Takahashi model fails at very low temperatures. This is also true in this example, where the temperature of 298.15 K is slightly below the critical temperature 304 K of CO_2.

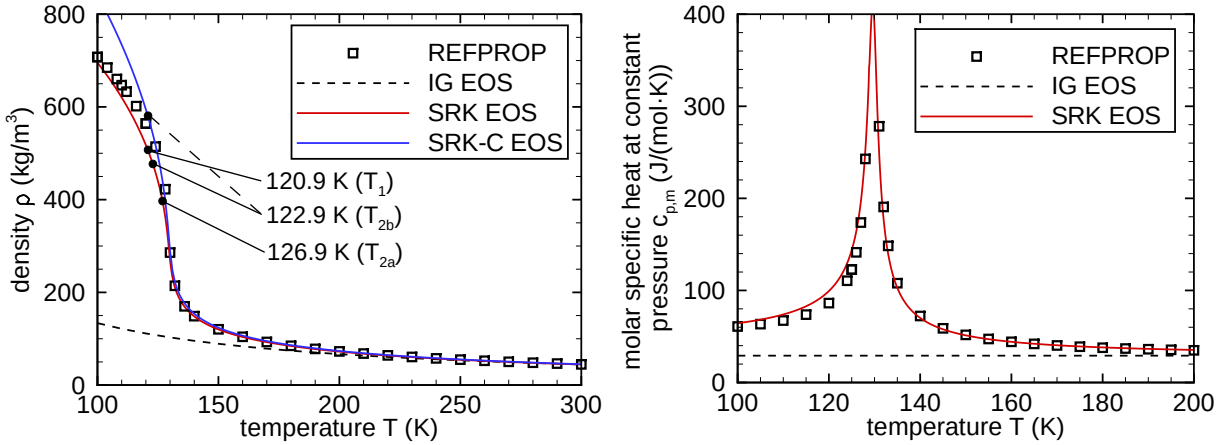

(a)

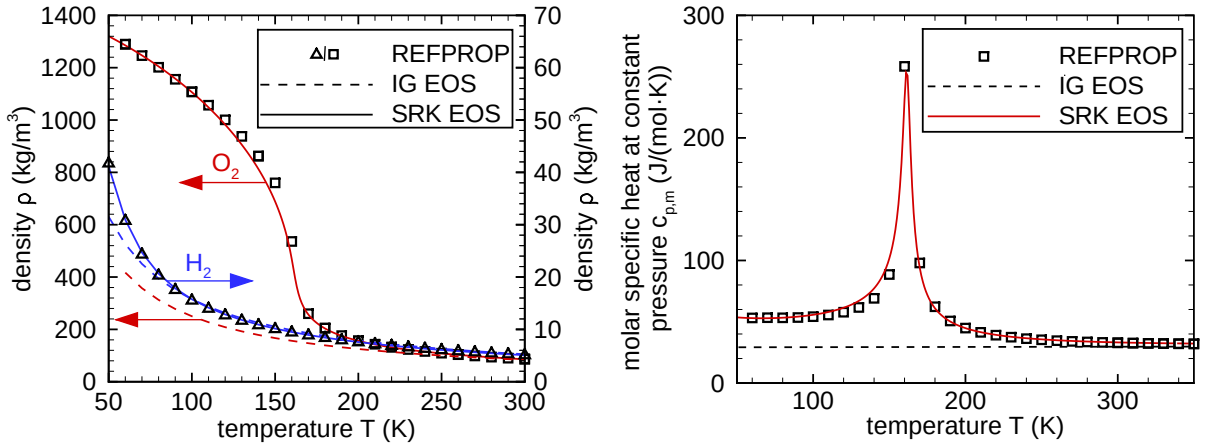

(b)

Figure 2: Density (left) and molar specific heat at constant pressure (right) for N_2 at 39.7 bar (a) as well as O_2 and H_2 at 65 bar (b) (only density plotted for H_2). Comparison of REFPROP correlations with properties calculated by the IG EOS, the SRK EOS, and optionally the SRK-C EOS.

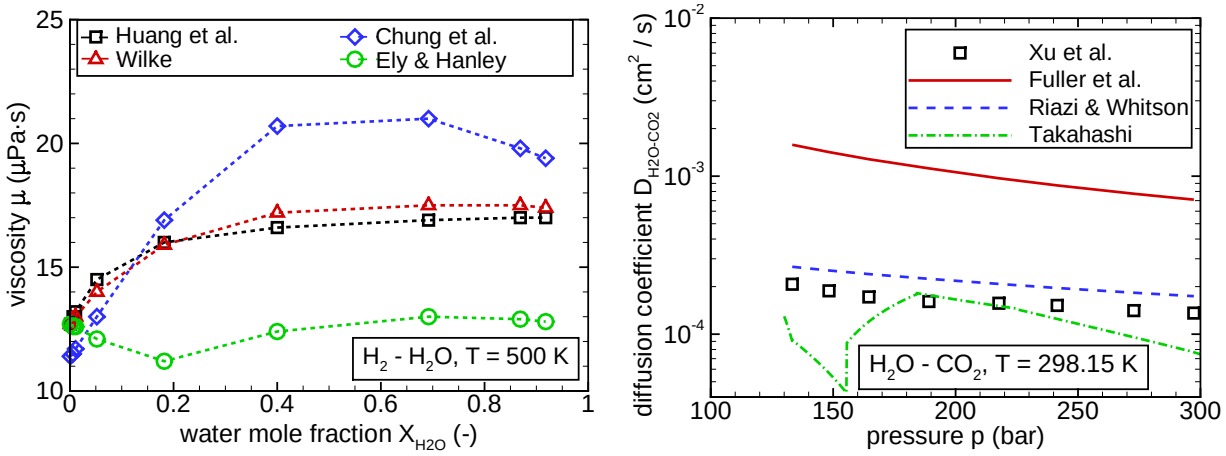

(a) (b)

Figure 3: Comparison of various models and experimental data: Ideal gas viscosity of H_2 - H_2O mixtures at 500 K (a) and high-pressure binary mass diffusion coefficients of H_2O in supercritical CO_2 at 298.15 K (b).

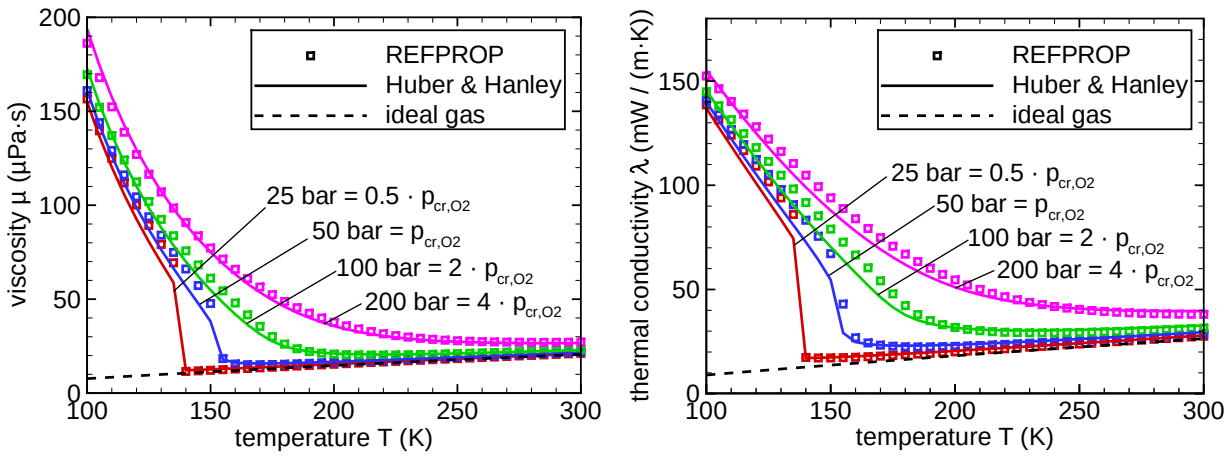

(a) (b)

Figure 4: Comparison of O_2 viscosity (a) and thermal conductivity (b) data from REFPROP with calculated values obtained with the model of Huber and Hanley [67] and ideal gas values from kinetic gas theory.

3 Governing equations and numerical method

3.1 Governing equations and physical models

In this work, the block-structured, finite-volume CFD code TASCOM3D [73] is applied to solve the 2D-axisymmetric or 3D extended Navier-Stokes equations for turbulent, reactive flows. The system of governing equations can be written as

$$\frac{\partial \left(y^{\delta}\mathbf{Q}_{\mathrm{c}}\right)}{\partial t} + \frac{\partial \left(y^{\delta}(\mathbf{F}_{\ell} - \mathbf{F}_{\ell}^{\nu})\right)}{\partial x_{\ell}} = \mathbf{S}\,, \tag{7}$$

where t is the physical time, x_{ℓ} the spatial coordinate in ℓ-direction, $y = x_2$ the radial coordinate in case of axisymmetric calculations with $\delta = 1$ (else $\delta = 0$), and $\mathbf{Q}_{\mathrm{c}}$ the conservative variable vector. $\mathbf{F}_{\ell}$ and $\mathbf{F}_{\ell}^{\nu}$ are the inviscid and viscous flux vectors in ℓ-direction and $\mathbf{S}$ is the source vector including terms for turbulence and chemical reactions. Einstein summation convention is used throughout this work.

Turbulence is modeled either via state-of-the-art RANS two-equation models (the q-ω [74], k-ω [75], and k-ω SST [76] models are in use) or by DDES [57]. The DDES is a hybrid URANS / LES approach, which combines advantages of both models, i. e. high accuracy and low demand on wall-parallel grid resolution within the boundary layer. In this work, the DDES model is used in combination with the k-ω turbulence model [77]. The DDES switches gradually from URANS mode in near-wall regions of boundary layers to LES mode in the outer boundary layer and core flow. Transition between both modes is accomplished by a modification of the turbulent length scale, which affects the dissipation term in the source term of the k-equation.

An FRC approach in combination with the detailed reaction mechanism from Ó Conaire et

al. [78] validated up to about 90 bar accounts for chemical reactions. Reactions are modeled by the source term vector using Arrhenius functions for the reaction rates and transport equations are solved for the main species O_2 and H_2 as well as for radicals OH, O, H, HO_2 and H_2O_2. The mass fraction of H_2O is obtained from $Y_{H_2O} = 1 - \sum_{\alpha=1}^{N_{sp}-1} Y_\alpha$, where N_{sp} is the number of considered species. With this, the conservative variable vector takes the form

$$\mathbf{Q}_c = \rho \left[1, \{u_\ell\}\,,\, e_{tot}\,,\, K\,,\, \omega\,,\, \{Y_\alpha\}\right]^T. \tag{8}$$

Indication of time-averaged (RANS) or filtered (LES) values is omitted in this paper. u_ℓ are velocity components in ℓ-direction, e_{tot} is the mass specific total energy, and K and ω are turbulence variabels. K either represents the modeled turbulent kinetic energy k in case of k-ω based turbulence models or its square root $q = \sqrt{k}$ in case of the q-ω model.

3.2 Time integration and preconditioning

For steady-state calculations, the physical time derivative in Eq. (7) is omitted. In case of time-accurate simulations, it is discretized with a second order backward differentiation formula (BDF) scheme. A time-marching technique is used for time integration [79]. To this end, an artificial time derivative term $\partial(y^\delta \mathbf{Q}_c)/\partial\tau$ is added to Eq. (7) to advance the solution in pseudo-time τ.

In regions of low Mach numbers $Ma = u/a_s \ll 1$ with a_s the isentropic speed of sound, the eigenvalues of the system (7) $u \pm a_s$ and u become disparate. The system of equations becomes very stiff, which is accompanied with severe convergence deterioration [80]. To improve convergence and eliminate problems due to eigenvalue stiffness at low Mach numbers, a preconditioning scheme similar to Zong and Yang is employed [5]. It has already successfully

been applied to ideal gas simulations with TASCOM3D [73] and was extended in this work to model real gas flows.

The preconditioning approach requires a modification of the speed of sound to scale all eigenvalues to the order of the convective speed u in the limit of incompressible flow. The speed of sound is defined as

$$a_\mathrm{s} \coloneqq \sqrt{\left(\frac{\partial p}{\partial \rho}\right)_s} = \sqrt{\frac{c_p}{c_v}\left(\frac{\partial p}{\partial \rho}\right)_T}\,, \tag{9}$$

where $(\partial p/\partial\rho)_s$ and $(\partial p/\partial\rho)_T$ are the isentropic and isothermal compressibility and c_v is the specific heat at constant volume. To gain excess to pressure and thus compressibility, integration in pseudo-time is changed to the primitive variable vector

$$\mathbf{Q}_\mathrm{p} = \left[p\,,\,\{u_\ell\}\,,\,T\,,\,K\,,\,\omega\,,\,\{Y_\alpha\}\right]^\mathrm{T}. \tag{10}$$

The discretized equations are solved by an implicit lower-upper symmetric Gauss-Seidel (LU-SGS) algorithm in the form of $\mathrm{LHS}\cdot\Delta\mathbf{Q}_\mathrm{p} = \mathrm{RHS}$. Here, the left- and right-hand side (LHS and RHS) represent the implicit and explicit part of the discretized system of equations and Δ constitutes the difference between two consecutive iterations in pseudo-time. In finite-volume formulation, this results in the following set of equations:

$$\underbrace{\left[y^\delta\left(\frac{\Omega}{\Delta\tau}\,\mathbb{I}^p + \frac{a_1\,\Omega}{\Delta t}\,\mathbb{T}^p + (\mathbb{J}^p_{\mathrm{F}_{\ell,f}} - \mathbb{J}^p_{\mathrm{F}^\nu_{\ell,f}})S_{\ell,f}\right) - \Omega\,\mathbb{J}^p_\mathrm{S}\right]}_{\mathrm{LHS}}\Delta\mathbf{Q}^p_\mathrm{p} = \tag{11}$$

$$\underbrace{\left[y^\delta\left(-\frac{\Omega}{\Delta t}\left(a_1\mathbf{Q}^p_\mathrm{c} + a_2\mathbf{Q}^n_\mathrm{c} + a_3\mathbf{Q}^{n-1}_\mathrm{c}\right) - (\mathbf{F}^p_{\ell,f}S_{\ell,f} - \mathbf{F}^{\nu,p}_{\ell,f}S_{\ell,f})\right) + \Omega\,\mathbf{S}^p\right]}_{\mathrm{RHS}}.$$

Here, Ω and S are the volume and surface area of a finite-volume cell, $\mathbb{J}_\mathrm{F}$, $\mathbb{J}_{\mathrm{F}^\nu}$, and $\mathbb{J}_\mathrm{S}$ are Jacobian matrices of the inviscid flux, the viscous flux, and the source term vector,

and $\mathbb{T}$ and $\mathbb{\Gamma}$ are the transformation and preconditioning matrix. The coefficients $a_1 = 1.5$, $a_2 = $-2 and $a_3 = 0.5$ originate from the second order BDF scheme. Subcripts ℓ and f indicate contributions in ℓ-direction and the respective cell surface. Supercripts n and p represent the physical time step and the iteration step in pseudo-time. The transformation matrix is defined as $\mathbb{T} = \partial \mathbf{Q}_\mathrm{c} / \partial \mathbf{Q}_\mathrm{p}$ and takes the following form:

$$
\mathbb{T} = \begin{bmatrix}
\theta_p & \{0\} & \theta_T & 0 & 0 & \left\{\theta_{Y_\beta}\right\} \\
\{u_\ell\, \theta_p\}^\mathrm{T} & [\,\rho\,] & \{u_\ell\, \theta_T\}^\mathrm{T} & \{0\}^\mathrm{T} & \{0\}^\mathrm{T} & \left[u_\ell\, \theta_{Y_\beta}\right] \\
h_\mathrm{tot}\theta_p + \frac{T}{\rho}\theta_T & \{\rho\, u_\ell\} & \rho c_p + h_\mathrm{tot}\theta_T & K' & 0 & \left\{h_\mathrm{tot}\theta_{Y_\beta} + \rho\,(\hat{h}_\beta - \hat{h}_{N_\mathrm{sp}})\right\} \\
K\,\theta_p & \{0\} & K\,\theta_T & \rho & 0 & \left\{K\,\theta_{Y_\beta}\right\} \\
\omega\,\theta_p & \{0\} & \omega\,\theta_T & 0 & \rho & \left\{\omega\,\theta_{Y_\beta}\right\} \\
\{Y_\alpha \theta_p\}^\mathrm{T} & [\,0\,] & \{Y_\alpha \theta_T\}^\mathrm{T} & \{0\}^\mathrm{T} & \{0\}^\mathrm{T} & \left[Y_\alpha\, \theta_{Y_\beta} + \rho\, \delta_{\alpha\beta}\right]
\end{bmatrix} \tag{12}
$$

with

$$
K' \coloneqq \frac{\partial(\rho e_\mathrm{tot})}{\partial K} = \begin{cases} 2\,\rho\, q & \text{for } K = q, \\ \rho & \text{for } K = k\,. \end{cases}
$$

Terms in [...] are submatrices and $\delta_{\alpha\beta}$ is the Kronecker delta. θ_p, θ_T, and θ_{Y_β} represent partial derivatives of ρ with respect to p, T, and Y_α while all other variables are held constant. Applying the preconditioner of Weiss and Smith [81], the preconditioning matrix takes a

similar form except that θ_p is replaced by the preconditioning factor $1/\beta$ with

$$\beta = \frac{f_\beta \, a_\mathrm{s}^2 \rho c_p}{\rho c_p + f_\beta a_\mathrm{s}^2 (T/\rho)\theta_T^2} = \frac{f_\beta \, a_\mathrm{s}^2}{1 + f_\beta (c_p/c_v - 1)}, \tag{13}$$

which scales with the local Mach number through the modulating function f_β [80]. The preconditioning factor artificially scales the local compressibility $(\partial p/\partial \rho)_T$ and thus the speed of sound, removing the stiffness of the system due to disparate eigenvalues. The modulating function varies in the range of [0;1] and is a function of the limited Mach number

$$\mathrm{Ma_o} = \min\Big[1, \max\big(\mathrm{Ma}, \epsilon_\mathrm{o}\big)\Big], \tag{14}$$

where ϵ_o is a lower bound to avoid divergence in regions of stagnation points (default value is 0.01 in this work). The lowest condition number with correct limiting behavior for $\mathrm{Ma} \to 0$ and $\mathrm{Ma} \to 1$ is obtained with [80]

$$f_\beta = \frac{2\,\mathrm{Ma_o^2}}{1 + \mathrm{Ma_o^2}}\,. \tag{15}$$

3.3 Spatial discretization scheme

The explicit viscous fluxes are discretized with a second order central discretization scheme. For the implicit part, a thin-layer approximation is applied [82]. The explicit inviscid fluxes are obtained through the use if Liou's [60] AUSM$^+$-up discretization scheme, whereas the inviscid flux Jacobian matrices are the derivatives of the analytical inviscid flux vector.

The AUSM$^+$-up scheme requires the left and right interpolated values at the interface of two neighboring cells. In this work, a high order upwind interpolation up to fifth order in space is used. To preserve monotonicity, a multidimensional TVD scheme from Kim and Kim [58] in the version of Gerlinger [59] termed MLP$^{\mathrm{ld}}$ is employed. In contrast to conventional TVD

limiters, values from cells of all directions and also diagonal neighboring cells are utilized, which increases the stability of the numerical scheme at low additional computational cost.

Concerning the AUSM$^+$-up scheme, two important points must be kept in mind when applying it in combination with a preconditioning scheme and a real gas framework. First, the AUSM$^+$-up scheme contains some diffusion terms that scale with the function

$$f_a = \mathrm{Ma_o}(2 - \mathrm{Ma_o})\,, \tag{16}$$

where $\mathrm{Ma_o}$ is named the reference Mach number and defined analogously to the limited Mach number of the preconditioning scheme in Eq. (14) by

$$\mathrm{Ma_o} = \min\left[1\,,\, \max\left(\mathrm{Ma}\,,\, \mathrm{Ma_{co}}\right)\right]. \tag{17}$$

The cut-off Mach number $\mathrm{Ma_{co}}$ is a lower bound, which increases stability but lowers accuracy with increasing value. It should be set in accordance with the Mach number limitation ϵ_o of the preconditioning scheme in Eq. (14). Otherwise, the numerical scheme may become unstable and diverge, since the diffusive term in the AUSM$^+$-up scheme is not correctly scaled in regions of Mach numbers below the cut-off Mach number.

The second point is a necessary modification of the interface speed of sound $a_{\mathrm{s},1/2}$ used in the AUSM$^+$-up scheme in case of real gases. In the paper of Liou [60], $a_{\mathrm{s},1/2}$ is determined from the critical speed of sound

$$a_\mathrm{s}^* = \frac{2\,(c_p/c_v - 1)}{c_p/c_v + 1}\, h_\mathrm{tot}\,. \tag{18}$$

However, this formula is only valid for perfect gases (constant specific heats). For ideal gases (temperature-dependent specific heats), an equivalent adiabatic exponent may be used to approximate the ratio c_p/c_v [83]. In case of real gases (temperature- and pressure-dependent

specific heats), the modification proposed by Edwards [84] is used in this work. $a_{\mathrm{s},1/2}$ is then directly calculated from left (L) and right (R) interface values of the density and speed of sound according to

$$a_{\mathrm{s},1/2} = \sqrt{\frac{\rho_{\mathrm{L}} a_{\mathrm{s,L}}^2 + \rho_{\mathrm{R}} a_{\mathrm{s,R}}^2}{(\rho_{\mathrm{L}} + \rho_{\mathrm{R}})}}\,. \tag{19}$$

4 Turbulent N_2 - Jet

The first validation test case "RCM-1" from the group of Mayer at the DLR test site in Lampoldshausen [10, 13] is a nonreacting, transcritically injected N_2 jet disintegrating into a N_2 environment at 298.15 K and 39.7 bar. The cold N_2 enters the pressurized chamber, which is 1 m in length and 122 mm in diameter, with a mean velocity of about 5 m/s ($Ma \approx 0.02$). The injector diameter d is 2.2 mm at the exit.

Injection temperatures were measured in separate test runs via thermocouples within the injector (120.9 K at position T_1 in Fig. 5) and at the injector exit. For the latter, thermocouples were either inserted orthogonally to the centerline (126.9 K at position T_{2a}) or 1 mm into the injector parallelly to the main flow direction (122.9 K at position T_{2b}). Measured temperatures vary due to heat transfer within the injector and probably intruding warm N_2 in the disturbed flow field in case of position T_{2a}. Further, measurement errors contribute to uncertainties in the injection temperatures. Though differences in temperatures are only minor, respective densities vary significantly in this thermodynamic region close to the pseudo-critical temperature (cf. Fig. 2(a)).

Axial and radial density profiles are available from the experiment. The measured densities at the centerline close to the injector exit are about 400 kg/m^3, which corresponds well with densities predicted by the SRK EOS at a temperature of $T_{2a} = 126.9$ K. However, when comparing with REFPROP correlations, experimental temperature and density data within the dense N_2 core are inconsistent with a bias of measured densities towards lower values.

Simulations were either performed by steady-state 2D axisymmetric RANS or time-accurate DDES with a full 3D model. The number of finite-volume elements of the computational

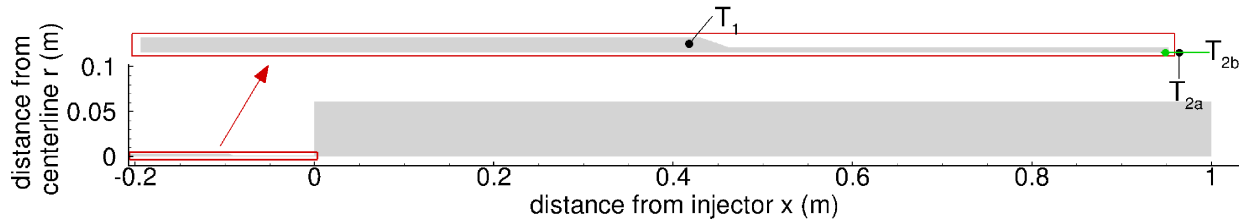

Figure 5: Computational domain (grey shaded areas) with close-up of the injector (red boxes) and positions of temperature measurements for the RCM-1 test case.

grids is 95 000 and 8 000 000, respectively. Cells are clustered towards the injector walls and chamber face plate to obtain a normalized wall distance of $y^+ \leq 1$. The physical time step in case of the DDES is 10^{-6} s. About one flow-through time was simulated before starting statistical time-averaging of results. Time-averaged results were obtained for a period of 0.1 s, which roughly corresponds to three flow-through times for normalized axial distances $x/d < 40$ from the injector exit. Convergence of the density residual by three orders of magnitude was accomplished in 12 to 14 inner iterations.

All boundary conditions were set in accordance with recommendations of the IWRCM-2 [48]. Block velocity and temperature profiles are set at the injector inlet for all test cases in this work. The turbulent intensity at the inlet is assumed to be 5 %, though results were insensitive to the chosen value for reasonable values below 10 %. The SRK EOS was used together with an injection temperature of $T_{2a} = T_{inj} = 126.9$ K for all RANS simulations and one DDES named "DDES-1" to match experimental densities at the injector exit. Influence of the injection temperatures and densities were investigated in a second DDES named "DDES-2" with $T_{2b} = T_{inj} = 122.9$ K. The more accurate SRK-C EOS with a volume correction of $c = +7.0 \cdot 10^{-6}$ m^3/mol (see section 2) was used in this case to better fit REFPROP correlations.

Figure 6 shows density and temperature contours for the 2D RANS simulation with the k-ω SST model. The high temperature dependency close to the pseudo-critical point results in large spatial density gradients. At position $x \approx 0.035$ m, temperature at the centerline has increased by 6 K only in the simulation, though density has already decreased by a factor of two.

Due to the very high turbulent viscosity in the RANS simulations (ratio of turbulent to molecular viscosity $\mu_t/\mu \approx \mathcal{O}(100) - \mathcal{O}(1\,000)$) and its damping effect, all RANS simulations remained steady even on significantly finer grids. To investigate unsteady phenomena observed in the experiment, DDES were performed in addition to RANS simulations. Numerical schlieren images (spatial density gradients) and the density isosurface at 400 kg/m^3 colored by the density gradient are pictured in Fig. 7 for the simulation DDES-2 in the range $x/d < 12$. The turbulent viscosity is drastically reduced in the core flow ($\mu_t/\mu \approx \mathcal{O}(10)$) and hydrodynamic instabilities evolve.

At the beginning, almost symmetric ring-like vortices are formed (indicated by arrows in Fig. 7), which finally disintegrate chaotically into smaller turbulent structures. Ring-structured vortex shedding was also confirmed in LES of Schmitt et al. [38] and Petit et al. [41], though Park [28] observed this only in combination with the inappropriate ideal gas law, but not with the SRK EOS. Qualitatively, the coherent structures in the DDES resemble those of comparable LES from Schmitt et al. [38], Park [28], Petit et al. [41], and Müller et al. [42].

To assess the quality of the DDES, the spectrum of resolved turbulent kinetic energy $E_k = 0.5\, u_i' u_i'$ (a prime indicating deviations form the mean value) is obtained by fast Fourier transform (FFT) and plotted in Fig. 8 for a monitor point within the shear layer. The

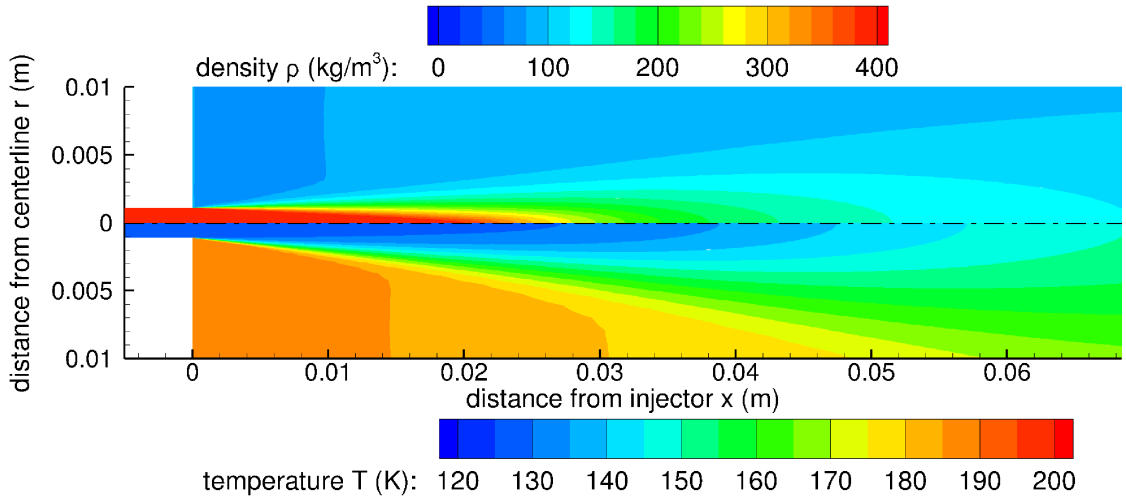

Figure 6: Density (top) and temperature (bottom) contours for the q-ω RANS simulation of the RCM-1 test case.

characteristic decay of resolved kinetic energy towards higher frequencies with a slope of -5/3 is observed, indicating a well-resolved flow field [85].

A quantitative comparison of axial and radial density profiles is presented in figures 9 and 10. Normalized densities $\rho^* = (\rho - \rho_{\min})/(\rho_{\max} - \rho_{\min})$ are plotted to allow a reasonable comparison at different injection temperatures and densities.

Concerning the densities along the centerline, the RANS simulation with the k-ω model predicts the decay of density too far downstream compared to experimental data from Branam and Mayer [13]. With the q-ω and k-ω SST model, the length of the dense core at the axis is reproduced well. However, the successive decay further downstream is too slow for the q-ω model, whereas an excellent match is obtained with the k-ω SST model. For the DDES-1 simulation, the dense core is predicted slightly too short in case of the same injection temperature of $T_{2a} = 126.9$ K, though for $x/d > 12$ DDES results closely follow experimental and k-ω SST densities. Since the temperature T_{2a} is probably higher than

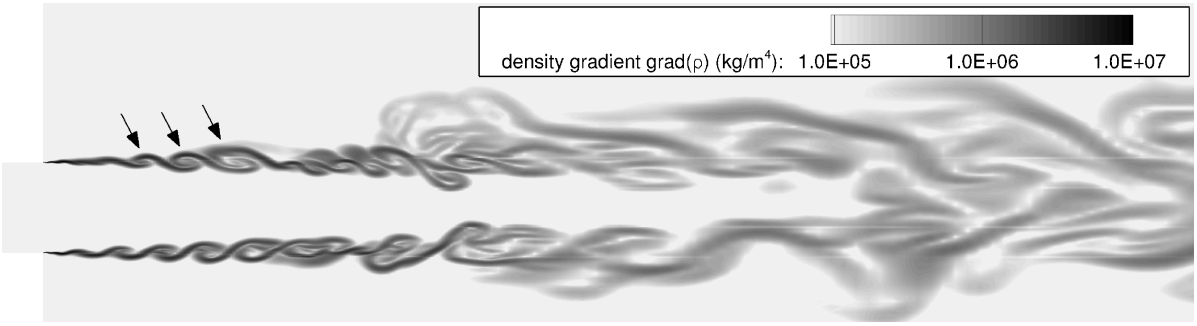

(a)

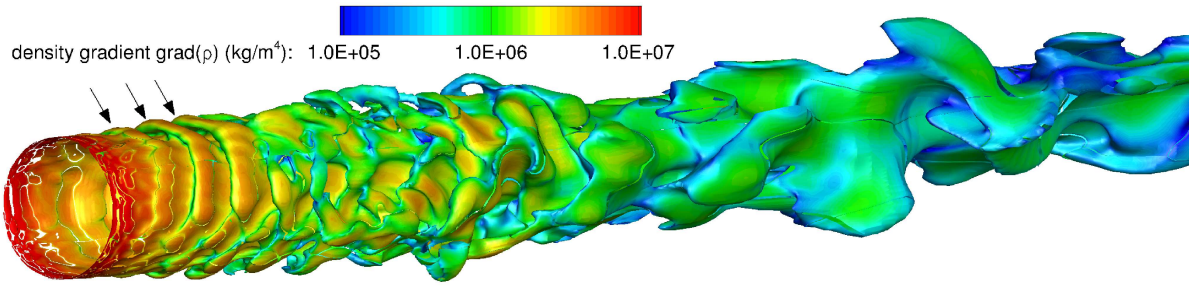

(b)

Figure 7: Spatial density gradients (numerical schlieren image) (a) and isocontour of density at 400 kg/m^3 colored by the spatial density gradient (b) for the DDES-2 simulation of the RCM-1 test case.

in the experiment, another simulation with $T_{2b} = 122.9$ K was conducted (DDES-2). With higher injection densities, the cryogenic core is more stable and disintegrates slightly further downstream compared to DDES-1 results.

The radial density profiles close to the injector at $x/d = 5$ (Fig. 10(a)) are less diffusive for all simulations in comparison with experimental data. Further downstream at $x/d = 25$ (Fig. 10(b)), only the k-ω shows significant deviations again. Considering the dispersion and uncertainties in experimental data, a good match with experimental data is obtained for simulations based on DDES, the k-ω SST model, and to some extend the q-ω model.

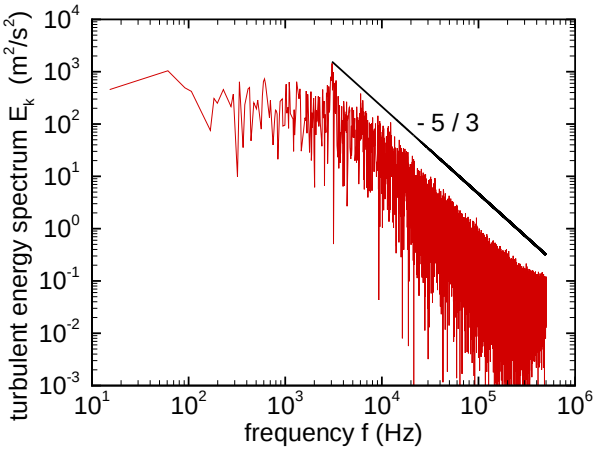

Figure 8: Spectrum of resolved turbulent kinetic energy within the shear layer for the DDES-2 simulation of the RCM-1 test case.

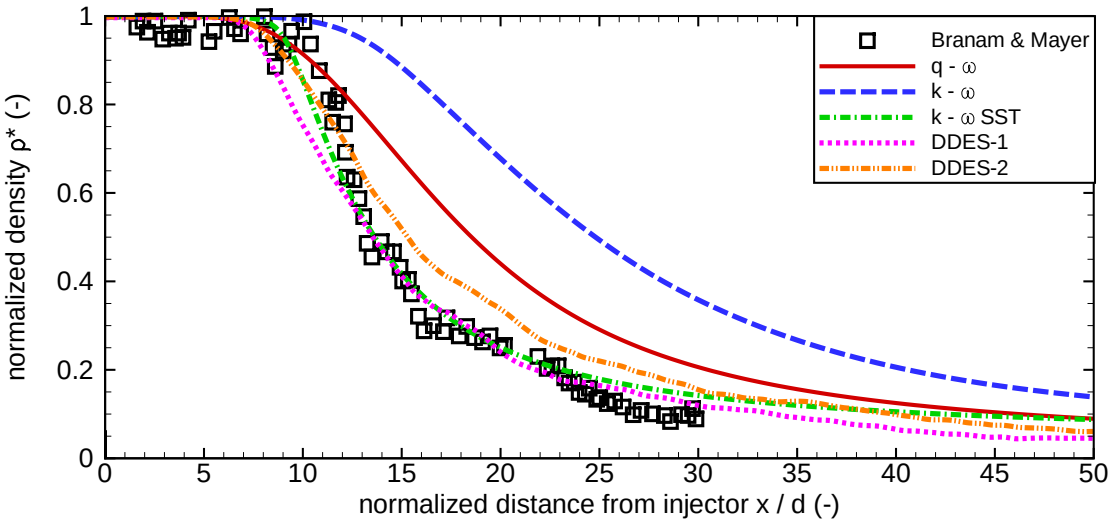

Figure 9: Comparison of experimental [10,13] and calculated axial density profiles along the centerline for the RCM-1 test case.

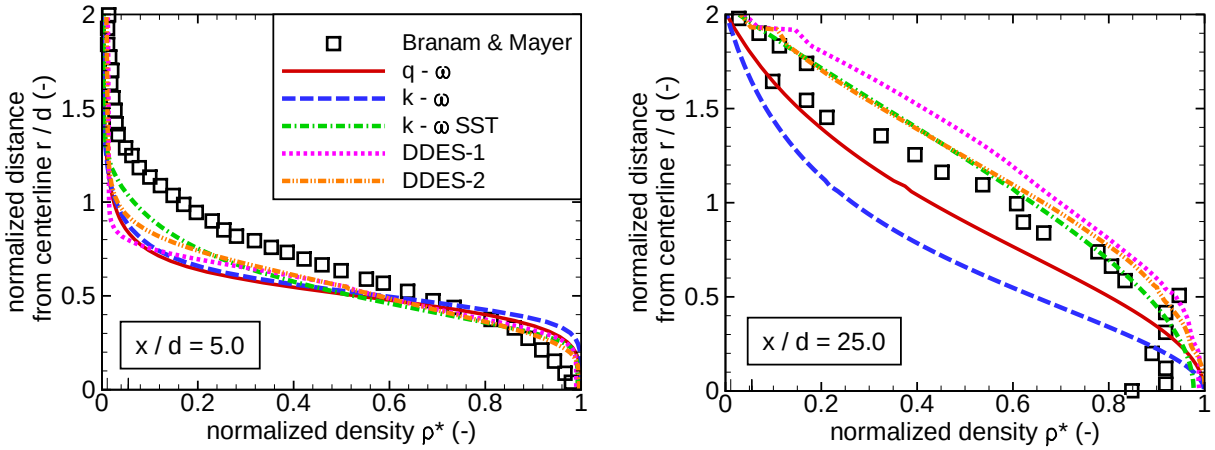

(a) (b)

Figure 10: Comparison of experimental [10, 13] and calculated radial density profiles at $x/d = 5$ (a) and $x/d = 25$ (b) for the RCM-1 test case.

5 Mascotte rocket combustor

The second validation test case "A-60" is concerned with high-pressure combustion of H_2 and O_2 in a rectangular model rocket combustor operated by ONERA at its test facility named MASCOTTE. The chamber length (injector to nozzle throat) is 477 mm and the cross section has an edge length of 50 mm. The nozzle throat is 9 mm in diameter. The chamber pressure is about 65 bar. (Various publications referring to the test case "A-60" with slightly different operating conditions exist, stating pressures between 60 and 70 bar [18,21,49].) The propellants are injected through a single shear coaxial injector. Liquid(-like) O_2 (LOX) is injected transcritically at a cryogenic temperature of 85 K through the inner duct, which has an exit diameter of 5 mm and is slightly chamfered at the exit. H_2 is injected at 287 K through the outer duct with inner and outer diameters of 5.6 and 10 mm, respectively. The chamber is operated fuel-rich with a ratio of oxydizer-to-fuel injector mass flow rate (O/F_{inj}) of 1.43 (equivalence ratio 5.56). The chamber provides optical access through quartz windows, which are cooled by a helium film of unknown temperature and mass flow rate. OH^* chemiluminescence images and CARS temperature measurements are available from the experiment.

All performed simulations are steady-state 2D axisymmetric RANS simulations, which have almost exclusively been employed for this test case in previous studies [6,24,29–33,47,50–53]. The chamber diameter in the simulation was set to 28.21 mm to preserve the chamber volume. The computational domain and grid details are plotted in Fig. 11. The grid consists of about 63 500 cells. The injector tip is resolved with 31 elements. Cells are clustered towards the injector region and the walls to obtain values of $y^+ < 2$.

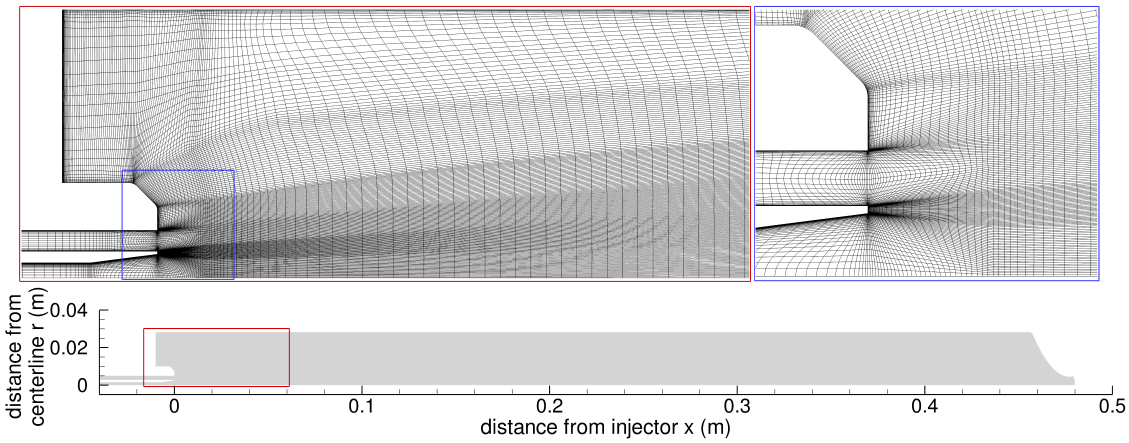

Figure 11: Computational domain and grid for the A-60 test case.

Boundary conditions are again set in accordance with recommendations of the IWRCM-2 [49]. The helium cooling film is neglected due to its unknown mass flow rate. Walls are assumed to be adiabatic. Isothermal chamber walls with wall temperature $T_\mathrm{w} = 500$ K were also tested but had little influence on the flow field and chamber pressure. The SRK EOS was used, which provides accurate thermodynamic correlations for the simulated operating conditions (see Fig. 2(b)).

A qualitative comparison between Abel transformed OH* emission intensities I_{OH^*} from the experiment, which indicate the reaction zone, and temperature contours for the simulation with the q-ω model gives a good match. The length of the flame is correctly reproduced, though the radial extension of the simulated flame seems larger than in the experiment. For simulations with the k-ω SST model the flame is closer to the axis like in the experiment, however, the dense LOX core and flame length are predicted too long (not shown here). In case of the k-ω model, no steady-state result could be obtained on this grid due to unsteady fluctuations in the flow field. This trend was also observed in simulations of other combustion chambers with transcritical and ideal gas injection conditions, e. g. test case 3 in this work.

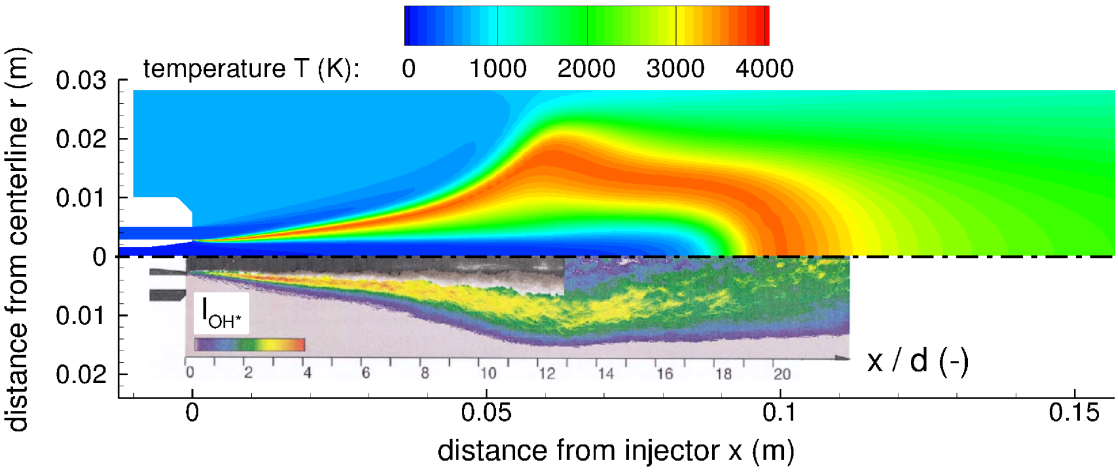

Figure 12: Comparison of calculated temperature contours obtained with the q-ω model and Abel transformed OH* intensities from the experiment [18] for the A-60 test case.

A quantitative comparison of axial and radial temperature profiles is presented in figures 13 and 14. An excellent match with experimental data is obtained with the q-ω model in terms of axial temperature profiles. As already mentioned, the k-ω SST model results in a too long flame. The temperature downstream of the reaction zone is higher with the k-ω SST model than with the q-ω model since less cool and abundant hydrogen is radially transported towards the centerline.

The radial temperature profiles of both simulations at a distance of 15 mm from the injector exit (Fig. 14(a)) are close to experimental values. Especially the temperature within the outer recirculation zone is captured well. The radial extension of the flame is closer to the centerline with the k-ω SST model, which is in slightly better accordance with experimental temperature measurements. From OH* emission images, the flame zone in the experiment is expected to be at about a distance of 3 to 4 mm from the centerline, which is confirmed for

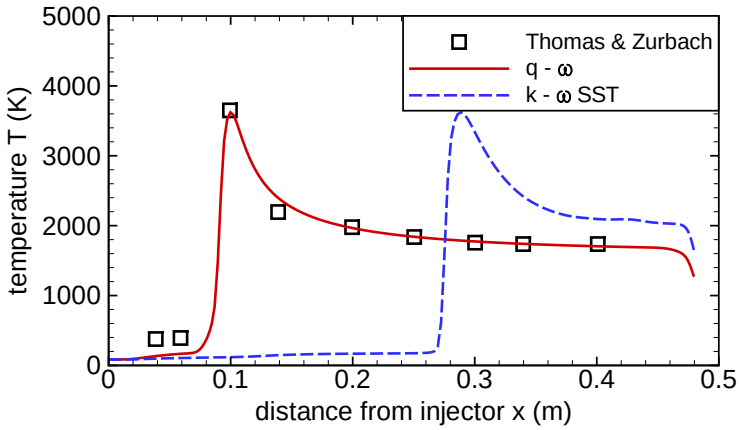

Figure 13: Comparison of experimental [49] and calculated axial temperature profiles for the A-60 test case.

both turbulence models. Further downstream at 50 mm from the injector (Fig. 14(b)), the temperatures in the outer zone towards the walls are still reproduced well in both simulations. The coarse distribution of temperature measurements does not capture the flame zone, but it indicates a relatively thin flame like in the simulation with the k-ω SST model. The q-ω acts more diffusive on the flow field and produces a much thicker flame than with the k-ω SST model and compared to the experiment.

Though all O_2 is consumed by reactions far upstream of the nozzle throat with both turbulence models, different chamber pressures were obtained in the simulations. In case of the q-ω simulation, the simulated chamber pressure is about 68.4 bar, higher than 63.7 bar obtained with the k-ω SST model. Both pressures are within the range of the reported chamber pressures in the experiments [18, 21, 49]. The reason for the different chamber pressures with both turbulence models can probably be attributed to differences in the flow field within the convergent-divergent nozzle (not shown here). The trend of higher chamber pressures with the q-ω model is also observed in test case 3.

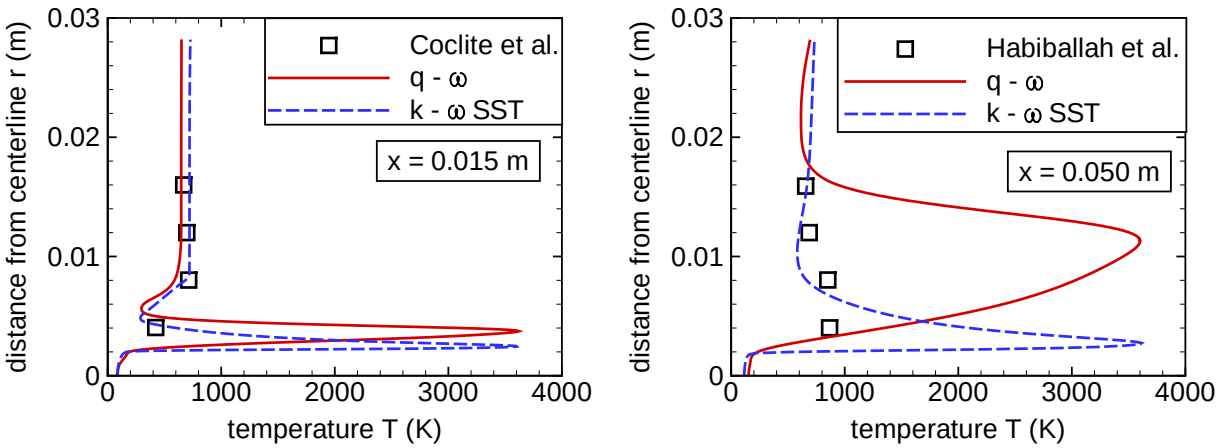

(a) (b)

Figure 14: Comparison of experimental and calculated radial temperature profiles for the A-60 test case. Experimental data taken from Coclite et al. [32] and Habiballah et al. [21].

6 DLR rocket combustor

The third validation test case "BKC" is similar to the second one. H_2 and O_2 are burnt at fuel-rich conditions and pressures of about 60 bar in a cylindrical model rocket combustor ("Brennkammer C") operated by DLR in Lampoldshausen [54, 55, 86]. The chamber length (injector to nozzle throat) is 430 mm and the chamber's diameter is 50 mm. The combustor is assembled from four interchangeable modules, one providing optical access. Further, it can be equipped with shear coaxial injectors of different size and varying nozzles. The nozzle throat is about 16.9 mm in diameter for the investigated test conditions. LOX and H_2 are again injected through the inner and outer duct of the injector. An H_2 cooling film protects the chamber walls.

Four different operating conditions are investigated in this work. Details are given in Tab. 1. Note that experimental operating conditions in [54, 55] differ slightly from the simulated test conditions 1 - 3, for which accurate boundary conditions were provided by the authors of [54, 55]. Injection temperatures for conditions 1 - 3 are very similar, but mass flows are varied to obtain different O/F ratios of 6, 5, and 4, respectively. For case 4, the O/F ratio is comparable to case 3 but injection temperatures are much lower. Deviations from the ideal gas behavior are even expected for H_2 close to the injector region (see Fig. 2(b)). Shadowgraph images are available from the experiment for conditions 1 - 3 allowing a comparison of the LOX core length [54, 55]. For condition 4, stronger pressure oscillations were noticed in the experiment and power spectral densities of pressure fluctuations are available for comparison [86].

Simulations for conditions 1 - 3 were performed with steady-state RANS employing the q - ω and k - ω SST model. Again, the k - ω model became unsteady. It was consequently used

Table 1: Details of operating conditions 1 - 4 for the BKC test case.

operating conditions	1	2	3	4
nominal chamber pressure (bar)	62	61	61	63
injector O/F ratio (-)	5.91	4.91	3.96	3.75
global O/F ratio (-)	1.32	1.22	1.12	0.97
injection temperature of O_2 (K)	113.0	112.7	112.8	95.7
injection temperature of H_2 (K)	151.3	153.2	155.0	66.7
temperature of H_2 cooling film (K)	313.0	318.0	320.5	320.5*

* Same value chosen as for condition 3 since actual value is unknown.

to model the unsteady behavior of condition 4. The same grid was used for all simulations (except for minor geometrical adaptations of the injector and nozzle geometry for condition 4) and consists of 324 000 elements, which are again strongly clustered towards the injector region and the walls. Boundary conditions are set analogously to the previous test cases. Walls are assumed to be adiabatic. The SRK EOS is used like for the A-60 test case.

Contours of density, temperature, as well as H_2 and O_2 mass fraction are presented in Fig. 15 for a simulation of condition 3 with the q-ω model. The strong cooling effect of the H_2 film is clearly visible from the temperature and H_2 mass fraction contours. The wall temperatures are kept below 600 K until the end of the cylindrical chamber section. For the k-ω SST model, the flame was observed to be thinner and less diffusive like in the A-60 test

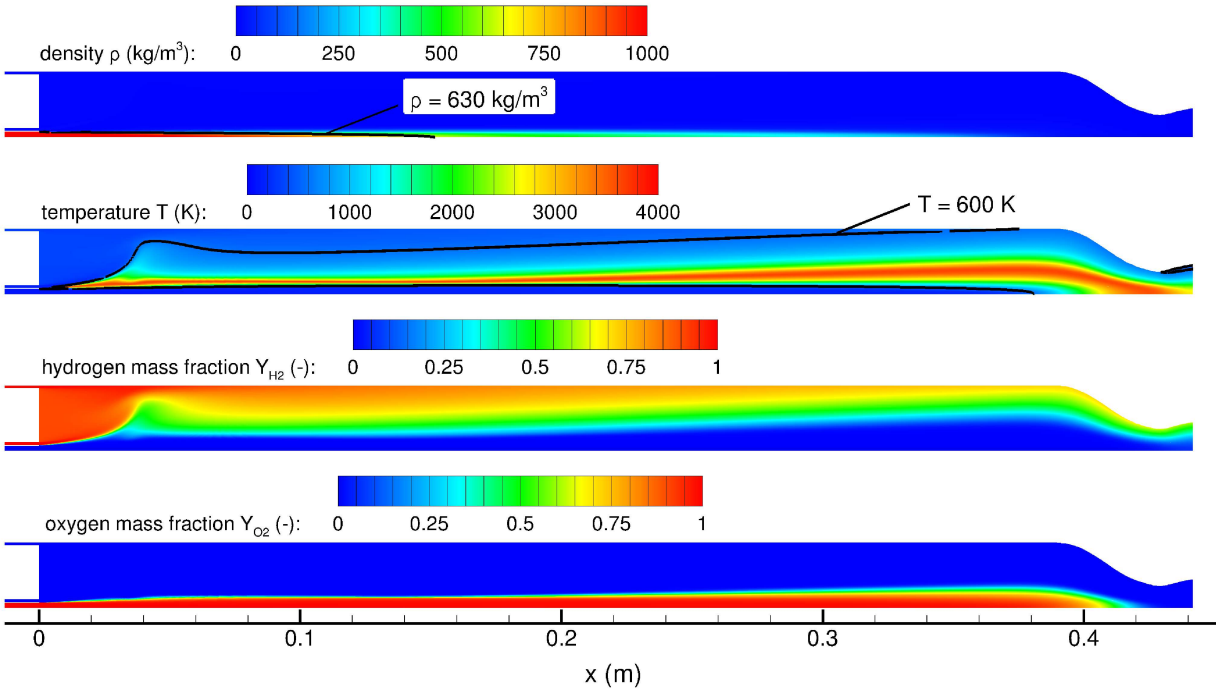

Figure 15: Contours of density, temperature, as well as H_2 and O_2 mass fraction (from top to bottom) for the simulation with the q-ω model of the BKC test case (condition 3).

case (not shown here).

The length of the dense LOX core and the flame are much longer than for the A-60 test case. The reaction zone partially extends into the nozzle in case of the q-ω solution. With the k-ω SST model, the reaction zone even reaches the nozzle exit and significant amounts of unburnt O_2 exit the combustor. As can be seen from density and O_2 mass fraction contours, unburnt gaseous O_2 prevails much further downstream than the visible dense LOX core, which was detected in the experiment downstream of 300 mm. Hence, it is likely that unburnt O_2 is also present at the nozzle exit in the experiment.

Time-averaged shadowgraph images were used to determine the mean length of the dense

LOX core L_{LOX} in the experiment. Presented shadowgraph images are, however, asymmetric and data evaluation is affected by strong uncertainties. Since the definition of the dense region is arbitrary, experimental results only allow a qualitative comparison of trends. For the CFD simulations, the dense core region is confined by the density isocontour at 630 kg/m^3 for the q-ω model and 760 kg/m^3 for the k-ω SST model by definition. The simulated LOX core length is determined as the axial distance between the injector exit and the position, where the respective density isocontour meets the centerline. The densities are chosen such that the simulated LOX core length corresponds with the measured dense LOX core length at condition 1 with O/F $\approx$ 6 in both cases. Though densities are close to the density of the pseudo-critical point (see Fig. 2(b)), where strong property variations occur, a qualitative comparison of the dense LOX core length is possible.

Figure 16(a) shows a comparison of the experimental and calculated mean LOX core length as defined before normalized by the LOX injector diameter d_{LOX}. The q-ω model correctly captures the trend of an increasing LOX core length with increasing O/F ratio. At an O/F ratio of 4, deviation to the experimental value is greater, however, than at O/F ratio 5. In contrast, the LOX core length remains roughly constant with the k-ω SST model and slightly decreases with increasing O/F ratio.

A comparison of experimental and simulated chamber pressures is illustrated in Fig. 16(b). The trend of a slightly increasing chamber pressure with increasing O/F ratio is reproduced well with both turbulence models. Whereas absolute pressures are very close to experimental values for the k-ω SST simulation, pressures are consistently higher for calculations with the q-ω model. This difference in pressure was already observed in test case 2. One contribution are again differences in the flow field within the convergent-divergent nozzle section (not

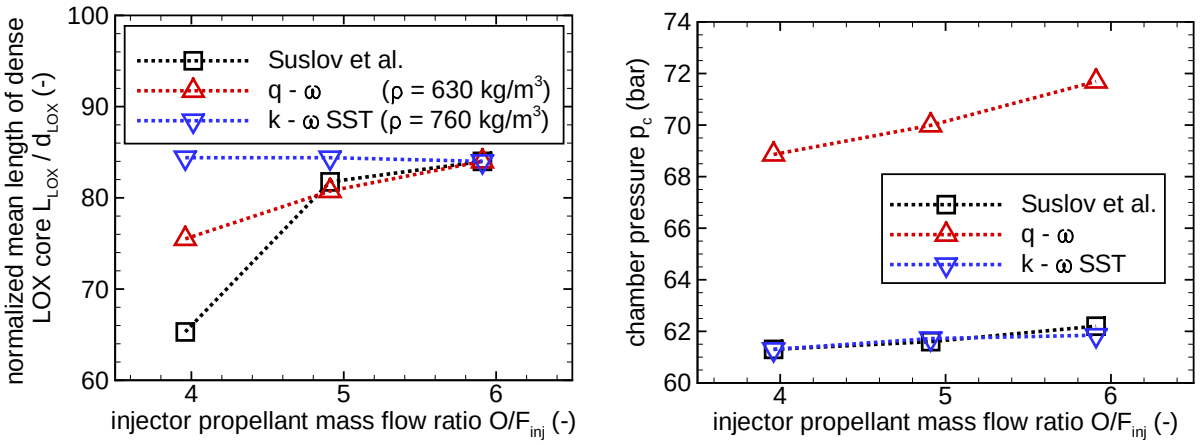

(a) (b)

Figure 16: Comparison of the experimental [54, 55] and calculated normalized mean length of the dense LOX core (a) and chamber pressure (b) for the BKC test case (conditions 1 - 3).

shown here). With the q-ω model, turbulent viscosity produced in the accelerating flow is about 2 to 5 times higher than with the k-ω SST model. Another contribution to the differences in chamber pressure is that significant amounts of unburnt O_2 exit the combustor in the k-ω SST simulation, whereas all O_2 is consumed in the q-ω solution.

A quantitative comparison of simulated wall temperatures for conditions 1 - 3 is presented in Fig. 17. As already mentioned, the H_2 cooling film effectively protects the walls from the intensive heat load of the flame. Simulations with the q-ω model predict very similar wall temperature distributions for all three operating conditions with slightly decreasing wall temperatures towards higher O/F ratios. Solutions with the k-ω SST are in very close agreement for O/F ratios 5 and 6. For an O/F ratio of 4, however, the model exhibits a much stronger sensitivity to the operating conditions than the q-ω model. The flame remains more confined to the centerline than with the q-ω model or at other O/F ratios and

wall temperatures are much lower.

For test condition 4, a time-accurate URANS simulation with the k-ω model was conducted. The physical time step was set to $5 \cdot 10^{-8}$ s. Data were collected for 0.1 s. About 22 inner iterations are required to reduce the density residual by three orders of magnitude. Fluctuations of the flow field remain mainly confined to the near-injector region ($x < 50$ mm) in the URANS simulation (not shown here). Nevertheless, the resulting pressure oscillations excite acoustic modes, which are captured by the URANS simulation.

Figure 18 compares experimental and simulated power spectral densities (PSD) of pressure fluctuations obtained by FFT for frequencies up to 9 000 Hz. The first, second, third, and fourth longitudinal mode (L1 - L4) were detected in the experiment at frequencies of about 1 750, 3 800, 5 700, and 7 550 Hz. The reason for the resonance observed at about 6 400 Hz is unkown. Smith et al. [86] denotes it a "pressure transducer cavity resonance", whereas it is attributed to vortex shedding of the cooling film by Smith [87]. In the URANS simulation, all longitudinal modes are reproduced, though at slightly higher frequencies than in the experiment. The amplitude of the L2 mode is predicted larger in the CFD but smaller for the other modes. All in all, a very satisfactory match with experimental data is attained.

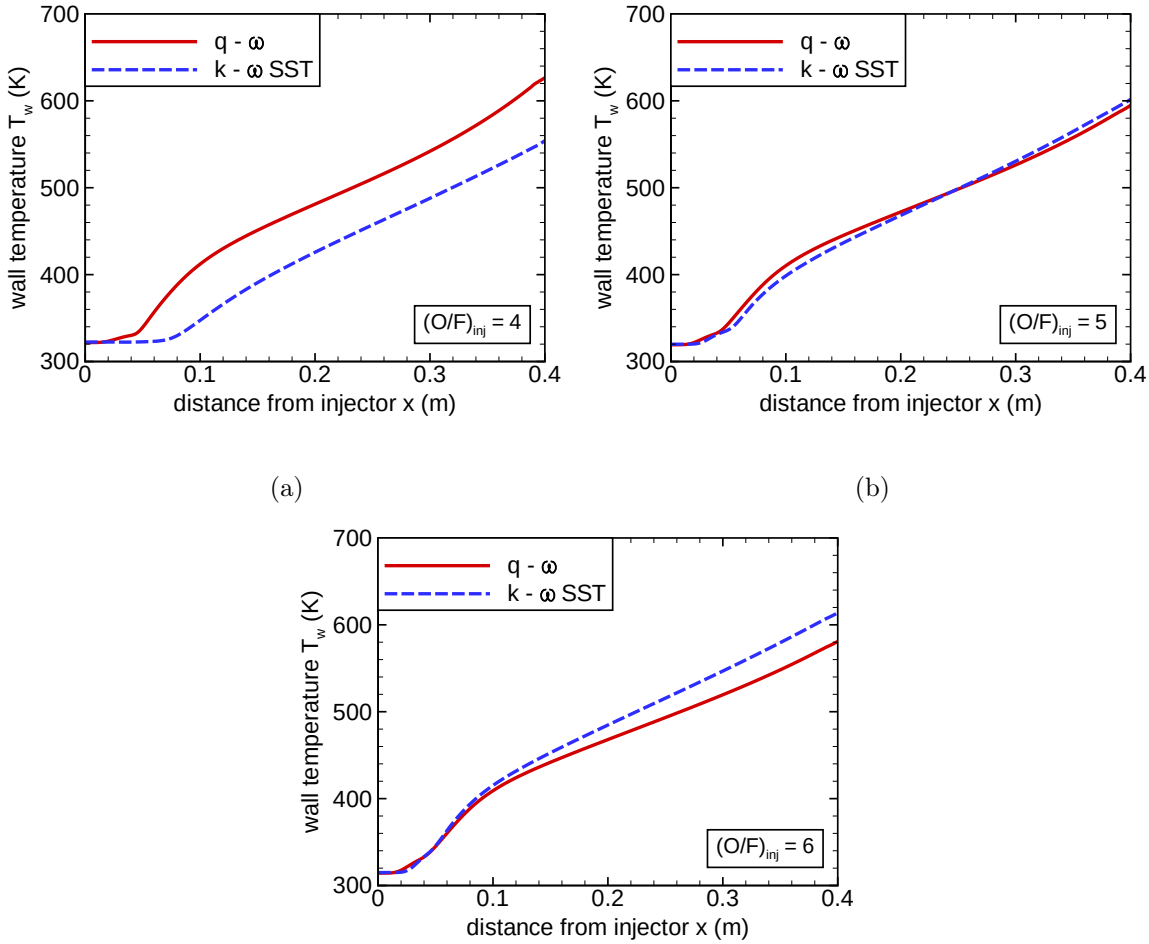

(a) (b)

(c)

Figure 17: Comparison of calculated wall temperatures for the BKC test case (conditions 1 - 3).

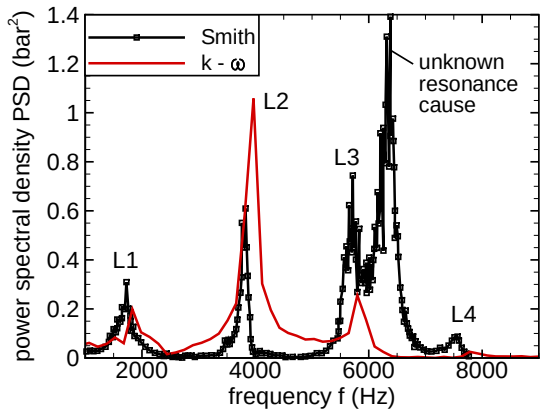

Figure 18: Comparison of experimental [86] and calculated power spectral densities of pressure fluctuations for the BKC test case (condition 4).

7 Conclusions

A consistent real gas framework based on a preconditioning scheme was implemented into the finite-volume CFD code TASCOM3D. Equations were derived to rigorously calculate all thermodynamic properties and partial derivatives from the reduced residual Helmholtz energy by use of fundamental thermodynamic relations. The SRK EOS, optionally with volume translation, provided an accurate representation of the thermodynamic behavior for the intended applications. High-pressure models of Huber and Hanley as well as Riazi and Whitson delivered values for fluid transport properties with sufficient accuracy. In contrast to other models commonly applied in literature, no unphysical behavior is observed in the entire thermodynamic range of interest. Also, high accuracy of the underlying ideal gas models is preserved in the limit of low densities.

Three test cases with transcritical injection were simulated: a non-reacting N_2 jet and H_2-O_2 combustion in two model rocket combustors with a single shear coaxial injector. Different turbulence modeling approaches were employed. Mainly RANS simulations based on two-equation turbulence models (q-ω, k-ω, and k-ω SST) with low computational cost were performed. To investigate unsteady effects, time-accurate URANS simulations and DDES were conducted. Except for a full 3D model in case of DDES, 2D axisymmetric grids were used. A good match with experimental data could be obtained for all test cases. However, no RANS turbulence model was able to reproduce all experimental data with high accuracy for all test cases. High order DDES results for the nonreacting test case are promising and reveal the potential of this hybrid URANS / LES approach for the application to reacting flows.

For the simulated nonreacting N_2 jet, RANS simulations with the k-ω SST and DDES were in excellent agreement with experimental density measurements. The q-ω model also delivered accurate results, but the k-ω model predicted the decay of density too far downstream. DDES results confirmed ring like vortex shedding prior to a chaotic disintegration of the jet like observed in previous numerical studies. Due to uncertainties of experimental injection temperature measurements and the high sensitivity of density w. r. t. temperature, an alternative injection temperature was investigated in another DDES. A lower injection temperature, i. e. a higher density, resulted in a more stable jet, which disintegrated slightly further downstream.

In case of the model rocket combustors, only 2D RANS and URANS simulations were performed due to high computing costs of reactive 3D DDES. Steady-state solutions were attained only with the q-ω and the k-ω SST model. The k-ω model was observed to act much less diffusive and the flow became unsteady. In simulations with the k-ω SST model, a thinner, less diffusive flame and a longer LOX core was observed compared to results with the q-ω model. Calculated chamber pressures in q-ω based solutions were consistently higher than with the k-ω SST model for both combustors.

For the Mascotte combustor, the simulated flame length and shape in the q-ω based solution were similar to experimental CARS temperature measurements and OH^* emission images, though the simulated flame is probably too diffusive. With the k-ω SST model, the flame length and LOX core seem to be too long, but the radial extend of the flame is probably closer to the experiment.

For the BKC combustor, simulations suggest that unburnt O_2 exits the combustor in the experiment. Chamber pressures are well reproduced with the k-ω SST model but consis-

tently higher in simulations with the q-ω model, where all O_2 is consumed upstream of the nozzle throat in contrast to the k-ω SST solution. A rather constant LOX core length for three different operating conditions with varying O/F ratio was detected for both turbulence models. The effective wall cooling with an H_2 film was confirmed in the simulations. Simulated wall temperatures for both turbulence models are in close agreement. URANS simulations with the k-ω model were conducted to simulate the acoustic behavior at operating conditions with very low injection temperatures for O_2 and H_2. The frequencies and amplitudes of the first four longitudinal modes measured in the experiment were satisfactorily reproduced.

Acknowledgments

Financial support was provided within the German Aerospace Center (Deutsches Zentrum für Luft- und Raumfahrt - DLR) project ProTau. The authors also wish to thank the German Research Foundation (Deutsche Forschungsgemeinschaft - DFG) for financial support within the “Sonderforschungsbereich Transregio 40”. Computational resources have been provided by the High Performance Computing Center Stuttgart (HLRS).

Appendix: properties derived from the reduced residual Helmholtz energy

The following formulae can be used to obtain all necessary thermodynamic properties and derivatives required in the CFD code by partial derivatives of the reduced residual Helmholtz energy Ψ. The procedure follows the work of Michelsen und Mollerup [56]. If the EOS is not given in its Helmholtz form but in its pressure-explicit form like the SRK-C EOS presented in section 2, the reduced residual Helmholtz energy must be evaluated from Eq. (4). Equations presented next are generally valid for all fluids and independent of the EOS in use.

For an EOS in the Helmholtz form, the pressure is obtained from Ψ with

$$p = -R_\mathrm{u} T \left(\frac{\partial \Psi}{\partial V}\right)_{T,\{n_\alpha\}} + \frac{R_\mathrm{u} T}{v_\mathrm{m}} \,. \tag{A.1}$$

The first order derivatives of pressure w. r. t. to volume, temperature, and species mole numbers are then given as

$$\left(\frac{\partial p}{\partial V}\right)_{T,\{n_\alpha\}} = -R_\mathrm{u} T \left(\frac{\partial^2 \Psi}{\partial V^2}\right)_{T,\{n_\alpha\}} - \frac{R_\mathrm{u} T}{n v_\mathrm{m}^2} \,, \tag{A.2}$$

$$\left(\frac{\partial p}{\partial T}\right)_{V,\{n_\alpha\}} = -R_\mathrm{u} T \left(\frac{\partial^2 \Psi}{\partial V \, \partial T}\right)_{\{n_\alpha\}} + \frac{p}{T} \,, \tag{A.3}$$

$$\left(\frac{\partial p}{\partial n_\alpha}\right)_{T,V,\{n_{\beta\neq\alpha}\}} = -R_\mathrm{u} T \left(\frac{\partial^2 \Psi}{\partial V \, \partial n_\alpha}\right)_{T,\{n_{\beta\neq\alpha}\}} + \frac{R_\mathrm{u} T}{n v_\mathrm{m}} \,. \tag{A.4}$$

Next, the partial molar volume, the natural logarithm of the fugacity coefficient φ, and its

partial derivative w. r. t. temperature can be evaluated:

$$\check{v}_\alpha := \left(\frac{\partial V}{\partial n_\alpha}\right)_{T,p,\{n_{\beta\neq\alpha}\}} = -\left(\frac{\partial p}{\partial n_\alpha}\right)_{T,V,\{n_{\beta\neq\alpha}\}} \Bigg/ \left(\frac{\partial p}{\partial V}\right)_{T,\{n_\alpha\}} , \tag{A.5}$$

$$\ln\varphi_\alpha = \left(\frac{\partial \Psi}{\partial n_\alpha}\right)_{T,V,\{n_{\beta\neq\alpha}\}} - \ln\left(\frac{p\, v_\mathrm{m}}{R_\mathrm{u} T}\right) , \tag{A.6}$$

$$\left(\frac{\partial\left(\ln\varphi_\alpha\right)}{\partial T}\right)_{p,\{n_\alpha\}} = \left(\frac{\partial^2 \Psi}{\partial T\, \partial n_\alpha}\right)_{V,\{n_{\beta\neq\alpha}\}} + \frac{1}{T} - \frac{\check{v}_\alpha}{R_\mathrm{u} T}\left(\frac{\partial p}{\partial T}\right)_{V,\{n_\alpha\}} . \tag{A.7}$$

With the residual partial molar enthalpy of species α

$$\check{h}^\mathrm{r}_\alpha = -R_\mathrm{u} T^2 \left(\frac{\partial\left(\ln\varphi_\alpha\right)}{\partial T}\right)_{p,\{n_\alpha\}} \tag{A.8}$$

the partial molar enthalpies are obtained from the ideal gas part (e. g. from NASA polynomials) and the residual part as

$$\check{h}_\alpha = h^\mathrm{IG}_{\mathrm{m},\alpha} + \check{h}^\mathrm{r}_\alpha . \tag{A.9}$$

Partial mass enthalpy and volume are easily calculated from their respective partial molar equivalents as

$$\hat{h}_\alpha = \check{h}_\alpha \,/\, M_\mathrm{w} , \tag{A.10}$$

$$\hat{v}_\alpha = \check{v}_\alpha \,/\, M_\mathrm{w} . \tag{A.11}$$

With the help of relation

$$\left(\frac{\partial \rho}{\partial v_\mathrm{m}}\right) = -\frac{M_\mathrm{w}}{v^2_\mathrm{m}} = -\frac{\rho^2}{M_\mathrm{w}} \tag{A.12}$$

the partial derivatives of density w. r. t. pressure, temperature, and species mass fractions, as required in the CFD code, can be connected to previously derived properties based on

extensive volume and mole numbers:

$$\left(\frac{\partial\rho}{\partial p}\right)_{T,\{Y_\alpha\}} = \frac{1}{n}\left(\frac{\partial\rho}{\partial v_\mathrm{m}}\right) \Bigg/ \left(\frac{\partial p}{\partial V}\right)_{T,\{n_\alpha\}} , \tag{A.13}$$

$$\left(\frac{\partial\rho}{\partial T}\right)_{p,\{Y_\alpha\}} = -\left(\frac{\partial\rho}{\partial p}\right)_{T,\{Y_\alpha\}} \left(\frac{\partial p}{\partial T}\right)_{V,\{n_\alpha\}} , \tag{A.14}$$

$$\left(\frac{\partial\rho}{\partial Y_\alpha}\right)_{T,p,\{Y_{\beta\neq\alpha}\}} = -\rho^2\left(\hat{v}_\alpha - \hat{v}_{N_\mathrm{sp}}\right) . \tag{A.15}$$

Finally, specific heats and the speed of sound are determined from

$$c_v = c_v^\mathrm{IG} - \frac{R_\mathrm{u}\,T}{nM_\mathrm{w}}\left[T\left(\frac{\partial^2\Psi}{\partial T^2}\right)_{V,\{n_\alpha\}} + 2\left(\frac{\partial\Psi}{\partial T}\right)_{V,\{n_\alpha\}}\right] , \tag{A.16}$$

$$c_p = c_v - \frac{T}{nM_\mathrm{w}}\left(\frac{\partial p}{\partial T}\right)^2_{V,\{n_\alpha\}} \Bigg/ \left(\frac{\partial p}{\partial V}\right)_{T,\{n_\alpha\}} , \tag{A.17}$$

$$a_\mathrm{s} := \sqrt{\left(\frac{\partial p}{\partial\rho}\right)_{s,\{n_\alpha\}}} = \sqrt{\frac{c_p}{c_v}\left(\frac{\partial p}{\partial\rho}\right)_{T,\{n_\alpha\}}} , \tag{A.18}$$

where the ideal gas part $c_v^\mathrm{IG} = c_p^\mathrm{IG} - R_\mathrm{u}$ can be evaluated from NASA polynomials. It should be noted that extensive mole numbers and volume only appear formally in the equations, but they are actually never used in the calculation.

For an efficient evaluation of equations A.1 - A.18, all composition dependence is put into the EOS parameters. For the SRK-C EOS (see section 2) with parameters $\mathcal{A} = \mathcal{A}(T,\{n_\alpha\})$, $\mathcal{B} = \mathcal{B}(\{n_\alpha\})$, and $\mathcal{C} = \mathcal{C}(\{n_\alpha\})$, the function $\Psi = \Psi(T,V,\{n_\alpha\})$ is then written as $\Psi = \Psi(n,T,V,\mathcal{A},\mathcal{B},\mathcal{C})$. The partial derivative of Ψ w. r. t. mole number of species α is then for example evaluated from

$$\left(\frac{\partial\Psi}{\partial n_\alpha}\right)_{T,V,\{n_{\beta\neq\alpha}\}} = \Psi_n + \Psi_\mathcal{A}\,\mathcal{A}_{n_\alpha} + \Psi_\mathcal{B}\,\mathcal{B}_{n_\alpha} + \Psi_\mathcal{C}\,\mathcal{C}_{n_\alpha} , \tag{A.19}$$

where X_y stands for the partial derivative of X w. r. t. y while holding all other variables from the set $n, T, V, \mathcal{A}, \mathcal{B}, \mathcal{C}$ constant. Though evaluation of all derivatives becomes tedious with increasing complexity of the EOS, the procedure is straightforward, efficient, and easy to implement and verify.

References

[1] E. Kiran, P. G. Debenedetti, C. J. Peters (editors), Supercritical fluids, Springer-Science+Business Media, B. V. (2000).

[2] V. Anikeev, M. Fan (editors), Supercritical fluid technology for energy and environmental applications, Elsevier B. V. (2014).

[3] Y. Oka, H. Mori (editors), Supercritical pressure light water cooled reactors, Springer Japan (2014).

[4] W. Ley, K. Wittmann, W. Hallmann, Handbuch der Raumfahrttechnik, 4th edition, Carl Hanser Verlag GmbH & Co. KG (2011).

[5] N. Zong, V. Yang, Cryogenic fluid jets and mixing layers in transcritical and supercritical environments, Combust. Sci. Technol. 178 (2006) 193–227.

[6] A. Ruiz, Simulations numériques instationnaires de la combustion turbulente et transcritique dans les moteurs cryotechniques, Ph.D. thesis, University Toulouse (2012).

[7] G. G. Simeoni, T. Bryk, F. A. Gorelli, M. Krisch, G. Ruocco, M. Santoro, T. Scopigno, The widom line as the crossover between liquid-like and gas-like behaviour in supercritical fluids, Nature Phys. 6 (2010) 503–507.

[8] B. E. Poling, J. M. Prausnitz, J. P. O'Connell, Properties of gases and liquids, 5th edition, McGraw-Hill Education, New York (2001).

[9] W. O. H. Mayer, A. H. A. Schik, B. Vielle, C. Chauveau, I. Gökalp, D. G. Talley,

R. D. Woodward, Atomization and breakup of cryogenic propellants under high-pressure subcritical and supercritical conditions, J. Propul. Power 14 (1998)(5) 835–842.

[10] W. Mayer, J. Telaar, R. Branam, Schneider. G., J. Hussong, Raman measurements of cryogenic injection at supercritical pressure, Heat Mass Transfer 39 (2003)(8) 709–719.

[11] R. Branam, J. Telaar, W. Mayer, Simulation of cryogenic jet injection, RCM 1, in O. Haidn (editor), Proceedings of the 2nd International Workshop on Rocket Combustion Modeling, 58 – 68.

[12] R. Branam, W. Mayer, Length scales in cryogenic injection at supercritical pressure, Exp. Fluids 33 (2002)(3) 422–428.

[13] R. Branam, W. Mayer, Characterization of cryogenic injection at supercritical pressure, J. Propul. Power 19 (2003)(3) 342–355.

[14] B. Chehroudi, R. Cohn, D. Talley, A. Badakhshan, Raman scattering measurements in the initial region of sub- and supercritical jets, AIAA Paper 2000-3392 (2000).

[15] B. Chehroudi, D. Talley, E. Coy, Visual characteristics and initial growth rates of round cryogenic jets at subcritical and supercritical pressures, Phys. Fluids 14 (2002)(2) 850–861.

[16] B. Chehroudi, R. Cohn, D. Talley, Cryogenic shear layers: experiments and phenomenological modeling of the initial growth rate under subcritical and supercritical conditions, Int. J. Heat Fluid Flow 23 (2002)(5) 554–563.

[17] W. Mayer, H. Tamura, Propellant injection in a liquid oxygen/gaseous hydrogen rocket engine, J. Propul. Power 12 (1996)(6) 1137–1147.

[18] M. Juniper, A. Tripathi, P. Scouflaire, J.-C. Rolon, S. Candel, Structure of cryogenic flames at elevated pressures, P. Comb. Inst. 28 (2000)(1) 1103 – 1109.

[19] O. J. Haidn, M. Habiballah, Research on high pressure cryogenic combustion, Aerosp. Sci. Technol. 7 (2003)(6) 473–491.

[20] S. Candel, M. Juniper, G. Singla, P. Scouflaire, C. Rolon, Structure and dynamics of cryogenic flames at supercritical pressure, Combust. Sci. Technol. 178 (2006)(1-3) 161–192.

[21] M. Habiballah, M. Orain, F. Grisch, L. Vingert, P. Gicquel, Experimental studies of high-pressure cryogenic flames on the Mascotte facility, Combust. Sci. Technol. 178 (2006)(1-3) 101–128.

[22] R. Farmer, G. Cheng, Y. S. Chen, CFD simulation of liquid rocket engine injectors: test case RCM-1, in O. Haidn (editor), Proceedings of the 2nd International Workshop on Rocket Combustion Modeling, 48–57.

[23] R. Blouquin, L. Lequette, The RCM-1 test case, a first attempt to model a supercritical cryogenic injection using the CPS code, in O. Haidn (editor), Proceedings of the 2nd International Workshop on Rocket Combustion Modeling, 69 – 86.

[24] L. Cutrone, Predicting reactive flows for propulsion applications using a flamelet/progress-variable approach, Ph.D. thesis, Italian Aerospace Research Center (CIRA) (2009).

[25] L. Cutrone, P. de Palma, G. Pascazio, M. Napolitano, A RANS flamelet/progress-variable method for computing reacting flows of real-gas mixtures, Comput. Fluids 39 (2010)(3) 485–498.

[26] D. T. Banuti, K. Hannemann, Effect of injector wall heat flux on cryogenic injection, AIAA Paper 2010-7139 (2010).

[27] T. Kim, Y. Kim, S.-K. Kim, Numerical study of cryogenic liquid nitrogen jets at supercritical pressures, J. Supercrit. Fluids 56 (2011)(2) 152–163.

[28] T. S. Park, LES and RANS simulations of cryogenic liquid nitrogen jets, J. Supercrit. Fluids 72 (2012) 232–247.

[29] M.-M. Poschner, M. Pfitzner, CFD-simulation of the injection and combustion of LOX and H_2 at supercritical pressures, AIAA Paper 2010-1144 .

[30] S. Pohl, M. Jarczyk, M. Pfitzner, B. Rogg, Real gas CFD simulations of hydrogen / oxygen supercritical combustion, Prog. Propul. Phys. 4 (2013) 583–614.

[31] M. M. Jarczyk, Numerische Modellierung von turbulenten Strömungen realer Gasgemische, Ph.D. thesis, Universität der Bundeswehr München (2013).

[32] A. Coclite, L. Cutrone, P. De Palma, G. Pascazio, Numerical investigation of high-pressure combustion in rocket engines using flamelet/progress-variable models, 53rd AIAA Aerospace Sciences Meeting (2015).

[33] D. T. Banuti, V. Hannemann, K. Hannemann, B. Weigand, An efficient multi-fluid-

mixing model for real gas reacting flows in liquid propellant rocket engines, Combust. Sci. Technol. 168 (2016) 98–112.

[34] A. Benmansour, A. Liazid, P.-O. Logerais, J.-F. Durastanti, A 3D numerical study of LO_2/GH_2 supercritical combustion in the ONERA-Mascotte test-rig configuration, J. Therm. Sci. 25 (2016)(1) 97 – 108.

[35] Meng. H., V. Yang, A unified treatment of general fluid thermodynamics and its application to a preconditioning scheme, J. Comput. Phys. 189 (2003) 277–304.

[36] V. Yang, Liquid-propellant rocket engine injector dynamics and combustion processes at supercritical conditions, Technical report, Department of Mechanical Engineering, The Pennsylvania State University (2004).

[37] J. C. Oefelein, Mixing and combustion of cryogenic oxygen-hydrogen shear-coaxial jets flames at supercritical pressure, Combust. Sci. Technol. 178 (2006)(1-3) 229–252.

[38] T. Schmitt, L. Selle, A. Ruiz, B. Cuenot, Large-eddy simulation of supercritical-pressure round jets, AIAA J. 48 (2010)(2) 2133–2144.

[39] M. M. Masquelet, Large-eddy simulations of high-pressure shear coaxial flows relevant for H_2-O_2 rocket engines, Ph.D. thesis, Georgia Institute of Technology (2013).

[40] J.-P. Hickey, M. Ihme, Supercritical mixing and combustion in rocket propulsion, Annual Research Briefs - 2013 (2013) 21–36.

[41] X. Petit, G. Ribert, G. Lartigue, P. Domingo, Large-eddy simulation of supercritical fluid injection, J. Supercrit. Fluids 84 (2013) 61–73.

[42] H. Müller, C. A. Niedermeier, J. Matheis, M. Pfitzner, S. Hickel, Large-eddy simulation of nitrogen injection at trans- and supercritical conditions, Phys. Fluids 28 (2016)(1).

[43] R. S. Miller, K. G. Harstad, J. Bellan, Direct numerical simulations of supercritical fluid mixing layers applied to heptane-nitrogen, J. Fluid Mech. 436 (2001) 1–39.

[44] N. Okong'o, J. Bellan, Real-gas effects on mean flow and temporal stability of binary-species mixing layers, AIAA J. 41 (2003)(12) 2429–2443.

[45] J. Bellan, Theory, modeling and analysis of turbulent supercritical mixing, Combust. Sci. Technol. 178 (2006)(1-3) 253–281.

[46] H. Terashima, M. Koshi, Strategy for simulating supercritical cryogenic jets using high-order schemes, Comput. Fluids 85 (2013) 39–46.

[47] G. C. Cheng, R. Farmer, Real fluid modeling of multiphase flows in liquid rocket engine combustors, J. Propul. Power 22 (2006)(6) 1373 – 1381.

[48] J. Telaar, G. Schneider, J. Hussong, W. Mayer, Cryogenic jet injection: description of test case RCM-1, in O. Haidn (editor), Proceedings of the 2nd International Workshop on Rocket Combustion Modeling, 42 – 47.

[49] J. L. Thomas, S. Zurbach, Presentation of test case RCM-3: supercritical spray combustion at 60 bar, in O. Haidn (editor), Proceedings of the 2nd International Workshop on Rocket Combustion Modeling.

[50] A. Depoutre, S. Zurbach, D. Saucereau, J. P. Dumont, E. Bodèle, I. Gökalp, Rocket combustion modelling test case RCM-3. Numerical calculation of MASCOTTE 60 bar

test case with THESEE, in O. Haidn (editor), Proceedings of the 2nd International Workshop on Rocket Combustion Modeling, 261 – 271.

[51] J. Görgen, O. Knab, Application of Astrium's CryoROC code to a single injector problem. A contribution to the RCM-3 Mascotte test case [60 bar], in O. Haidn (editor), Proceedings of the 2nd International Workshop on Rocket Combustion Modeling, 253 – 260.

[52] B. Legrand, P. Durand, P. Vuillermoz, Test case RCM-3 using CPS, in O. Haidn (editor), Proceedings of the 2nd International Workshop on Rocket Combustion Modeling, 239– 252.

[53] A. Benarous, A. Liazid, H_2-O_2 supercritical combustion modeling using a CFD code, Therm. Sci. 13 (2009)(3) 139–152.

[54] D. I. Suslov, J. S. Hardi, B. Knapp, M. Oschwald, Hot-fire testing of LOX/H_2 single coaxial injector at high pressure conditions with optical diagnostics, 6th European Conference for Aeronautics and Space Science (EUCASS) (2015).

[55] D. I. Suslov, J. S. Hardi, B. Knapp, M. Oschwald, Optical investigation of the LOX-jet disintegration processes at high pressure conditions in a LOX/H_2 single coaxial injector combustion chamber, Space Propulsion Conference Paper SP2016 3124815 (2016).

[56] J. M. Michelsen, M. L. Mollerup, Thermodynamic models: fundamentals & computational aspects, 2nd edition, Tie-Line Publications (2007).

[57] P. Spalart, S. Deck, M. Shur, K. Squires, M. Strelets, A. Travin, A new version of

detached-eddy simulation, resistant to ambigous grid densities, Theoret. Comput. Fluid Dynamics 20 (2006)(3) 181–195.

[58] K. H. Kim, C. Kim, Accurate, efficient and monotonic numerical methods for multi-dimensional compressible flows. part II: multi-dimensional limiting process, J. Comput. Phys. 208 (2005)(2) 570–615.

[59] P. Gerlinger, Multi-dimensional limiting for high-order schemes including turbulence and combustion, J. Comput. Phys. 231 (2012) 2199–2228.

[60] M.-S. Liou, A sequel to AUSM, part II: AUSM$^+$-up for all speeds, J. Comput. Phys. 214 (2006)(1) 137–170.

[61] A. Péneloux, E. Rauzy, R. Freze, A consistent correction for Redlich-Kwong-Soave volumes, Fluid Phase Equilib. 8 (1982) 7–23.

[62] E. W. Lemmon, M. L. Huber, M. O. McLinden, NIST standard reference database 23: reference fluid thermodynamic and transport properties-REFPROP, version 9.1, National Institute of Standards and Technology, Gaithersburg (2013).

[63] J. F. Ely, H. J. M. Hanley, Prediction of transport properties. 1. viscosity of fluids and mixtures, Ind. Eng. Chem. Fundam. 20 (1981) 323–332.

[64] J. F. Ely, H. J. M. Hanley, Prediction of transport properties. 2. thermal conductivity of fluids and mixtures, Ind. Eng. Chem. Fundam. 22 (1983) 90–97.

[65] T.-H. Chung, M. Ajlan, L. L. Lee, K. E. Starling, Generalized multiparameter correlation

for nonpolar and polar fluid transport properties, Ind. Eng. Chem. Res. 27 (1988) 671–679.

[66] S. Takahashi, Preparation of a generalized chart for the diffusion coefficients of gases at high pressures, J. Chem. Eng. Jpn. 7 (1974)(6) 417–420.

[67] M. L. Huber, H. J. M. Hanley, 12 The corresponding-states principle: dense fluids, in J. Millat, J. H. Dymond, C. A. Nieto de Castro (editors), Transport properties of fluids, their correlation, prediction and estimation, Cambridge University Press, 283–295.

[68] M. R. Riazi, C. H. Whitson, Estimating diffusion coefficients of dense fluids, Ind. Eng. Chem. Res. 32 (1993) 3081–3088.

[69] C. R. Wilke, The viscosity of gas mixtures, J. Chem. Phys. 18 (1950)(4) 517–519.

[70] P. H. Huang, Accurate determination of the hydrogen-water viscosity in PEMFC, ECS Trans. 30 (2011)(1) 33–40.

[71] E. N. Fuller, F. Ensley, J. C. Giddings, Diffusion of halogenated hydrocarbons in helium. The effect of structure on collision cross sections, J. Phys. Chem. 73 (1969)(11) 3679–3685.

[72] B. Xu, K. Nagashima, J. M. DeSimone, C. S. Johnson Jr., Diffusion of water in liquid and supercritical carbon dioxide: an NMR study, J. Phys. Chem. A 107 (2003)(1) 1–3.

[73] Y. H. Simsont, P. Gerlinger, High order numerical simulation of the thermal load on a lobed strut injector for scramjet applications, Int. J. Numer. Meth. Fluids, accepted for publication (2016).

[74] T. J. Coakley, Turbulence modeling for high speed flows, AIAA Paper 1997-0436 (1992).

[75] D. C. Wilcox, Formulation of the k-ω turbulence model revisited, AIAA J. 46 (2008)(11) 2823–2838.

[76] F. R. Menter, Zonal two equation k-ω turbulence models for aerodynamic flows, AIAA Paper 1993-2906 (1993).

[77] M. Kindler, Verbrennungssimulation in instationären kompressiblen Strömungen, Ph.D. thesis, Universität Stuttgart (2014).

[78] M. Ó Conaire, H. J. Curran, J. M. Simmie, W. J. Pitz, C. K. Westbrook, A comprehensive modeling study of hydrogen oxidation, Int. J. Chem. Kinet. 36 (2004) 603–622.

[79] S. Venkateswaran, C. L. Merkle, Dual time stepping and preconditioning for unsteady computations, AIAA Paper 1995-0078 (1995).

[80] S.-H. Lee, Effects of condition number on preconditioning for low mach number flows, J. Comput. Phys. 231 (2012)(10) 4001–4014.

[81] J. M. Weiss, W. A. Smith, Preconditioning applied to variable and constant density flows, AIAA J. 33 (1995)(11) 2050–2057.

[82] J.-S. Shuen, Upwind differencing and LU factorization for chemical non-equilibrium Navier-Stokes equations, J. Comput. Phys. 99 (1992)(2) 233–250.

[83] P. Gerlinger, Numerische Berechnung turbulenter Verbrennungsvorgänge mit einem impliziten LU-Verfahren, Ph.D. thesis, University Stuttgart (1995).

[84] J. R. Edwards, R. K. Franklin, M.-S. Liou, Low-diffusion flux-splitting methods for real fluid flows with phase transition, AIAA J. 38 (2000)(9) 1624–1633.

[85] S. B. Pope, Turbulent flows, Cambridge University Press (2000).

[86] J. Smith, D. Klimenko, W. Clauß, W. Mayer, Supercritical LOX/hydrogen rocket combustion investigations using optical diagnostics, AIAA Paper 2002-4033 (2002).

[87] J. J. Smith, High pressure rocket engine combustion, Ph.D. thesis, The University of Adelaide (2007).